ResearchGate

See discussions, stats, and author profiles for this publication at: https://www.researchgate.net/publication/383231645

Design and Evaluation of Tunable Terahertz Metasurface Biosensor for Malaria Detection with Machine learning Optimization Using Artificial Intelligence

Article *in* Plasmonics · August 2024

DOI: 10.1007/s11468-024-02491-2

CITATIONS
31

READS
335

4 authors, including:

Ngaira Mandela
National Forensic Sciences University
42 PUBLICATIONS **479** CITATIONS
SEE PROFILE

Obed Apochi
12 PUBLICATIONS **102** CITATIONS
SEE PROFILE

Abdessalem Bouhenna
Hassiba Benbouali University of Chlef
25 PUBLICATIONS **146** CITATIONS
SEE PROFILE

All content following this page was uploaded by Jacob Wekalao on 19 August 2024.

The user has requested enhancement of the downloaded file.

Plasmonics
https://doi.org/10.1007/s11468-024-02491-2

RESEARCH

Design and Evaluation of Tunable Terahertz Metasurface Biosensor for Malaria Detection with Machine learning Optimization Using Artificial Intelligence

Jacob Wekalao[1] · Ngaira Mandela[2] · Apochi Obed[3] · Abdessalem Bouhenna[4]

Received: 17 July 2024 / Accepted: 12 August 2024
© The Author(s), under exclusive licence to Springer Science+Business Media, LLC, part of Springer Nature 2024

Abstract
Malaria continues to be a major global health issue, impacting millions each year and leading to hundreds of thousands of deaths, especially in less developed areas. Timely and precise diagnosis is essential for effective treatment and management of this parasitic illness. This study presents the design and evaluation of a tunable terahertz (THz) metasurface biosensor tailored for malaria detection, integrating plasmonic materials with artificial intelligence. The biosensor employs a multi-layer structure comprising graphene, gold, and silver to leverage surface plasmon resonance effects. Comprehensive electromagnetic simulations and parameter optimization demonstrate the sensor's ability to detect minute changes in malaria parasite concentrations, achieving a peak sensitivity of 429 GHzRIU^{-1}, detection accuracy of 25.6 and a figure of merit of 10.989 RIU$_{-1}$. The sensor features tunable elements that allow dynamic performance adjustments. Additionally, the XGBoost machine learning algorithm is harnessed to predict sensor performance across various design parameters, consistently demonstrating maximum R^2 ranging up to 100%. This fusion of advanced materials, precise engineering, and predictive analytics represents a significant advancement in biosensing technology for malaria detection, offering substantial potential for early and accurate diagnosis.

Keywords Metasurfaces · Graphene · Machine learning · XGBoost · Quality factor · Biosensor

Introduction

Biosensors are analytical tools that integrates biological recognition elements with a physicochemical transducer [1]. The field of biosensing has garnered considerable interest owing to its diverse applications across numerous fields such as healthcare, environmental surveillance, food safety among others [2].The core function of a biosensors hinges on the precise interaction between the analyte and bioreceptor [3]. This binding event triggers a signal that is then converted by the transducer into a quantifiable output [4]. Two key performance parameters of biosensors are sensitivity and concentration [5]. Sensitivity reflects the device's capability to respond to minor fluctuations in analyte concentration. Selectivity, which denotes its ability to distinguish the target analyte from other potentially interfering substances [6].

Malaria is severe illness induced by Plasmodium parasites [7]. This disease still persists as a major global health obstacle [8]. Accurate and timely diagnosis is crucial for effective treatment and control strategies [9].The golden methods for diagnosing malaria involves the examination of Giemsa-stained blood smears under a microscope, facilitating the identification of species and the quantification of parasitaemia [10]. However, this technique necessitates skilled microscopists and may overlook low-level infections. To mitigate these challenges, rapid diagnostic tests have been developed [11]. These immunochromatographic assays identify specific Plasmodium antigens, such as histidine-rich

✉ Jacob Wekalao
jacob.phdfs2303@nfsu.ac.in

[1] School of Engineering and Technology, National Forensic Sciences University, Gandhinagar 382007, Gujarat, India

[2] School of Digital Forensics and Cyber Security, National Forensic Sciences University, Gandhinagar 382007, Gujarat, India

[3] School of behavioral sciences, National Forensic Sciences University, Gandhinagar 382007, Gujarat, India

[4] Department of theoretical physics and Material sciences, Hassiba Benbouali University of Chlef, Ouled Fares, Algeria

Published online: 19 August 2024

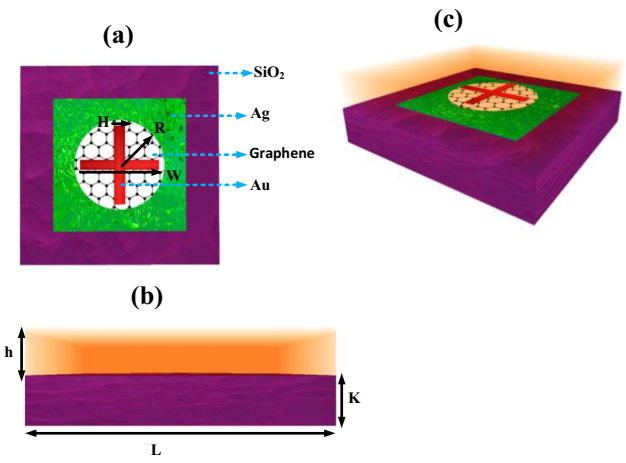

Fig. 1 depicts different perspectives of the suggested sensor design: (a) a top-down view, (b) a lateral view, and (c) a three-dimensional representation

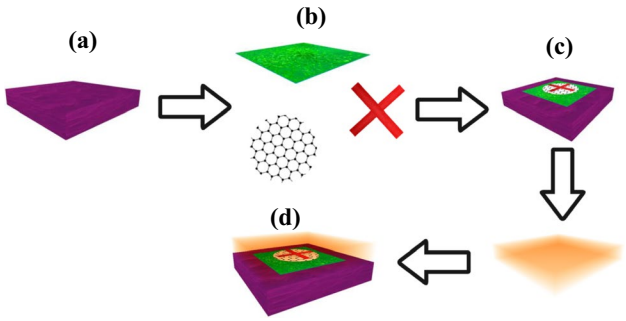

Fig. 2 illustrates the fabrication process of the proposed sensor

protein 2 for *P. falciparum* or *Plasmodium lactate* for all species, in a blood droplet within 15–30 min [12].

For enhanced sensitivity and specificity, molecular techniques such as polymerase chain reaction (PCR) are employed [13]. PCR facilitates the amplification of parasite DNA, with nested and real-time PCR techniques capable of detecting sub microscopic infections and distinguishing between species [14]. Another laboratory-based approach, enzyme-linked immunosorbent assay (ELISA), is employed to detect either parasite antigens or host antibodies [15]. Antigen-based ELISAs demonstrate greater specificity for active infections compared to antibody-based assays, which may indicate previous exposure [16]. While ELISAs exhibit high sensitivity, they are primarily suited for epidemiological investigations rather than individual diagnosis.

The underlying principle of metasurfaces revolves around their capacity to manipulate light-matter interactions on scales smaller than the wavelength of light [17]. Through precise customization of the geometry, dimensions, alignment, and material properties of meta-atoms, researchers have developed resonant configurations that exhibit pronounced interactions with incoming light [18]. These interactions give rise to localized phase alterations, spanning from 0 to 2π, within spatial extents significantly smaller than the wavelength [19]. This subwavelength control over phase enables the creation of planar optical elements, including lenses, holograms, beam deflectors, and polarization converters, all characterized by thicknesses on the order of hundreds of nanometres [20].

Over the past decade, a category of two-dimensional (2D) materials known as MXenes(MXs) has been developed [21]. First documented in 2011, MXs is derived from their three-dimensional (3D) precursors termed MAX phases [22]. In MAX phases, M denotes an early transition metal (such as Ti, Nb, Mo), A represents a group IIIA or IVA element (primarily Al), and X signifies either carbon or nitrogen. The distinctive structure and characteristics of MXenes, combined with their straightforward synthesis methods, render them exceptionally promising for a broad spectrum of applications [23, 24].In the field of biosensing, MXenes

Fig. 3 illustrates the operation of the proposed sensor

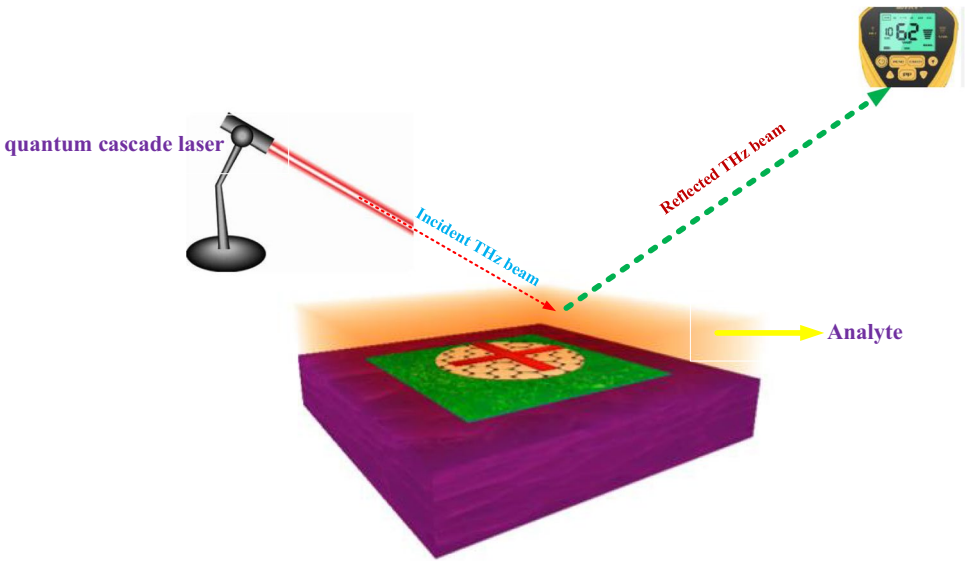

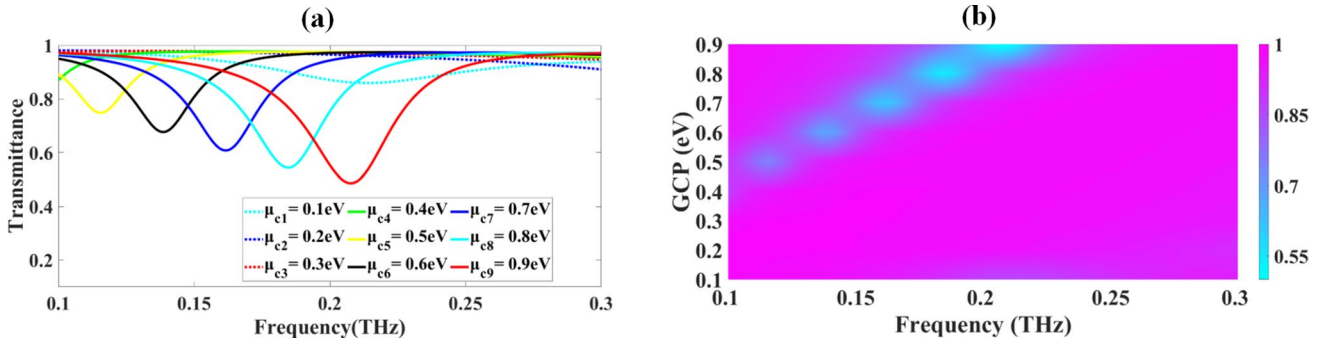

Fig. 4 shows how changes in GCP impact the transmittance response of the sensor design

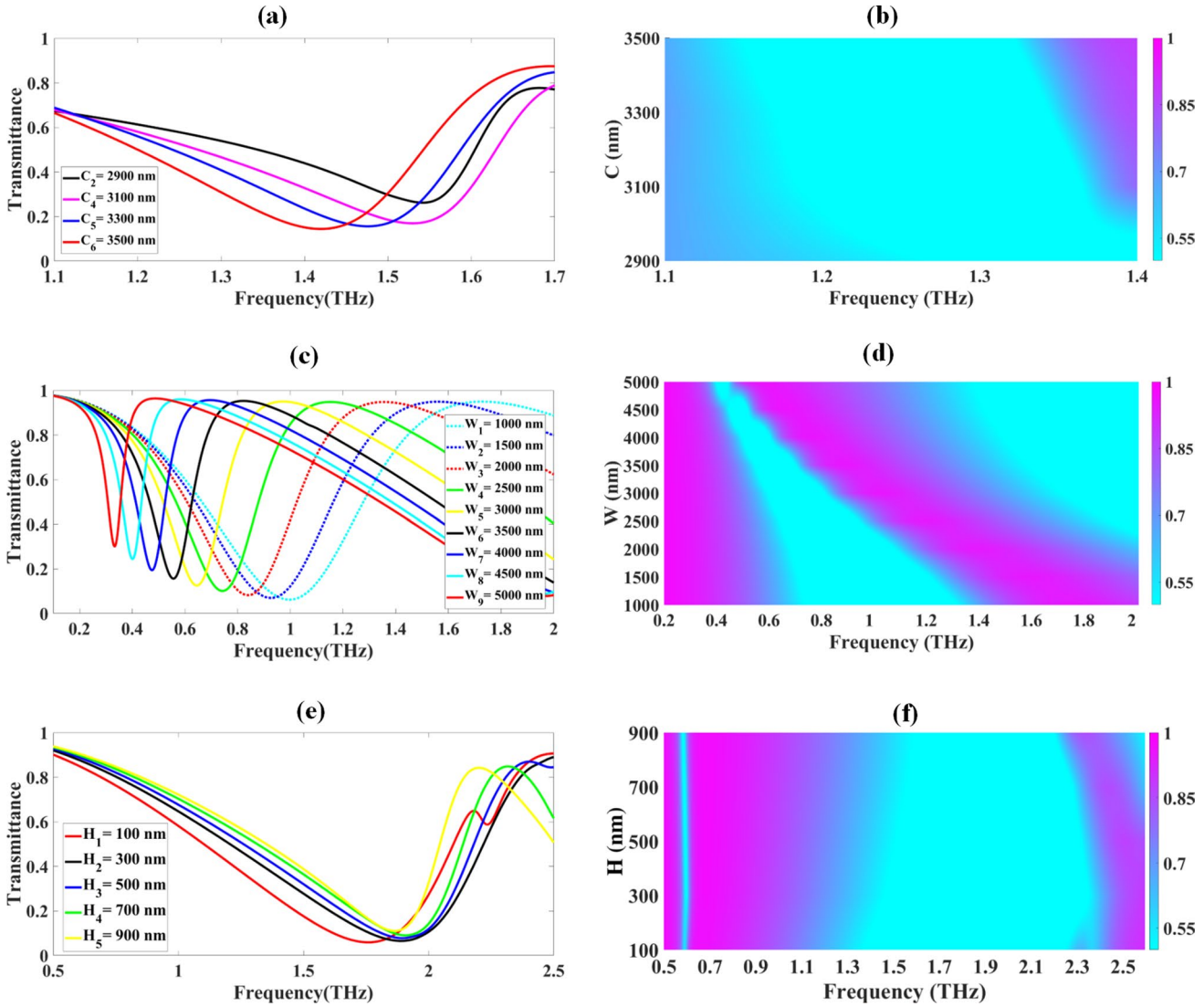

Fig. 5 depicts the impact of varying the dimensions of circular resonators and adjusting the width and height of rectangular resonators on the transmittance response

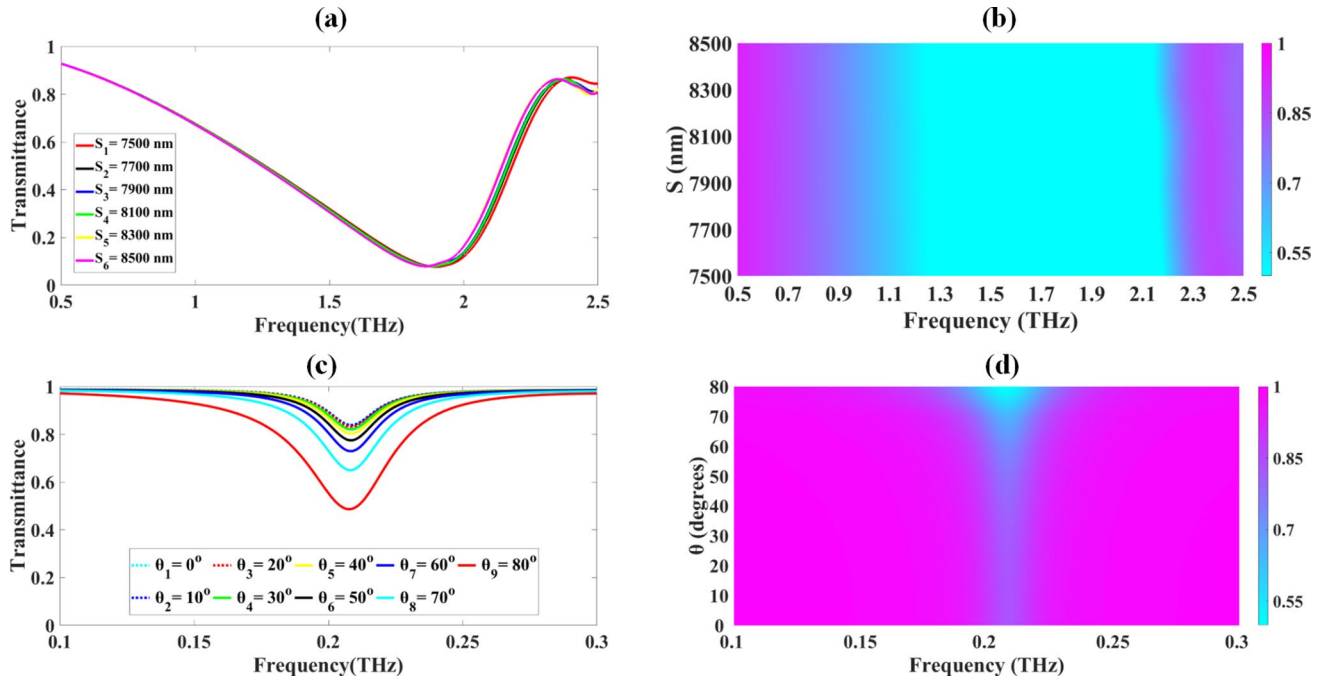

Fig. 6 presents an analysis of how variations in the dimensions of the square resonator and changes in the angle of incidence affect the transmittance response

have exhibited remarkable promise [25]. Their exceptional conductivity facilitates efficient electron transfer, thereby enhancing the performance of electrochemical sensors [26]. For example Yotsarayuth et al. presented a sensor based on $Ti_3C_2T_x$ MXene with superior capabilities in detecting temperature al [27].On the other hand, the surface functional groups of MXenes serve as ideal anchoring sites for biomolecules [28]. Through the functionalization of MXenes with enzymes, antibodies, or aptamers, researchers have engineered highly selective sensors for various targets including glucose, cancer biomarkers, and pathogens [29].

On the other hand, Phosphorus, acknowledged as an indispensable element for life due to its integral role in DNA, ATP, and phospholipids is also a crucial material in biosensing [30]. Although its biological significance is well-documented, the elemental form of phosphorus, particularly its allotropes, has gained considerable interest among materials scientists and bioengineers [31]. Among these allotropes, black phosphorus (BP) holds prominence due to its distinctive optoelectronic properties and its potential utility in various biosensing applications [32]. Black phosphorus exhibits a layered structure similar to graphite, yet its configuration differs due to sp_3 hybridization, resulting in a puckered, honeycomb lattice [33]. This distinctive structure imparts highly anisotropic properties, a characteristic not observed in graphene or many transition metal dichalcogenides (TMDs) [34]. Similar to graphene, black phosphorus can undergo exfoliation down to a single layer, referred to as phosphorene [35].

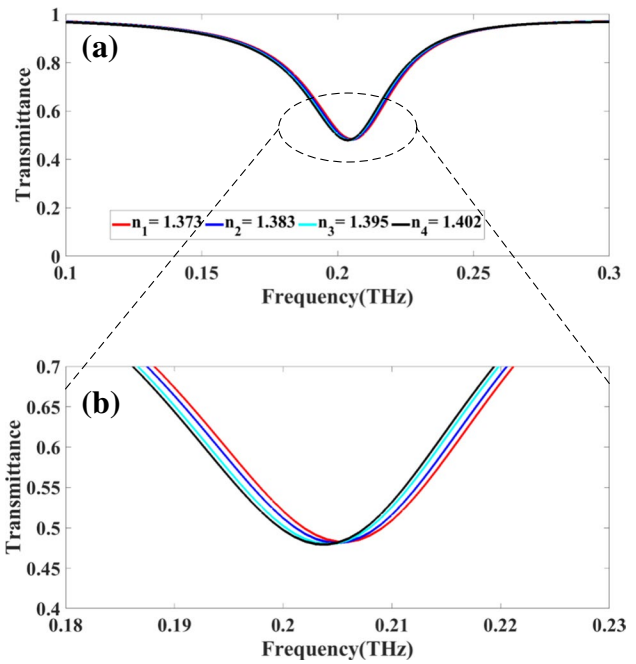

Fig 7 illustrate the relationship between fluctuations in transmittance response and variations in RIs associated with different concentration of malaria samples

This paper presents the design and theoretical analysis of a tunable THz metasurface biosensor for malaria detection. The proposed sensor exploits surface plasmon resonance

effects and the ability to dynamically tune the graphene conductivity to achieve high sensitivity to variations in the refractive index of malaria-infected blood samples. Through rigorous electromagnetic simulations and parameter optimization, we demonstrate the sensor's capability to detect subtle changes in refractive index corresponding to different malaria parasite concentrations. Furthermore, we employ the XGBoost machine learning algorithm to predict sensor behaviour across various design parameters.

Designing and Modelling

In this study, we employ COMSOL Multiphysics version 6.2 to conduct high-fidelity simulations of the proposed sensor design.The numerical analysis investigates the electromagnetic response under terahertz frequency excitation applied at discrete points along the z-axis. To accurately represent the periodic nature of the structure, we rigorously impose periodic boundary conditions in both the x and y directions. The geometric discretization utilizes a tetrahedral meshing algorithm with a minimum element size of 0.5 nm. This high-resolution meshing strategy ensures accurate representation of the sensor's geometrical features and facilitates precise numerical approximation of the electromagnetic field distributions.The proposed sensor design comprises two rectangular resonators positioned centrally within the structure. These rectangular resonators have dimensions: a length (W) of 3.72 µm and a width (H) of 0.5 µm. These two shapes are arranged to form a plus-shaped resonator. Surrounding these rectangular resonators is a circular resonator with a radius (R) of 3.5 µm. The entire assembly of resonators is mounted on a square resonator that spans 7.5 µm on each side. This square resonator serves as a foundational element for the arrangement of the other resonators.

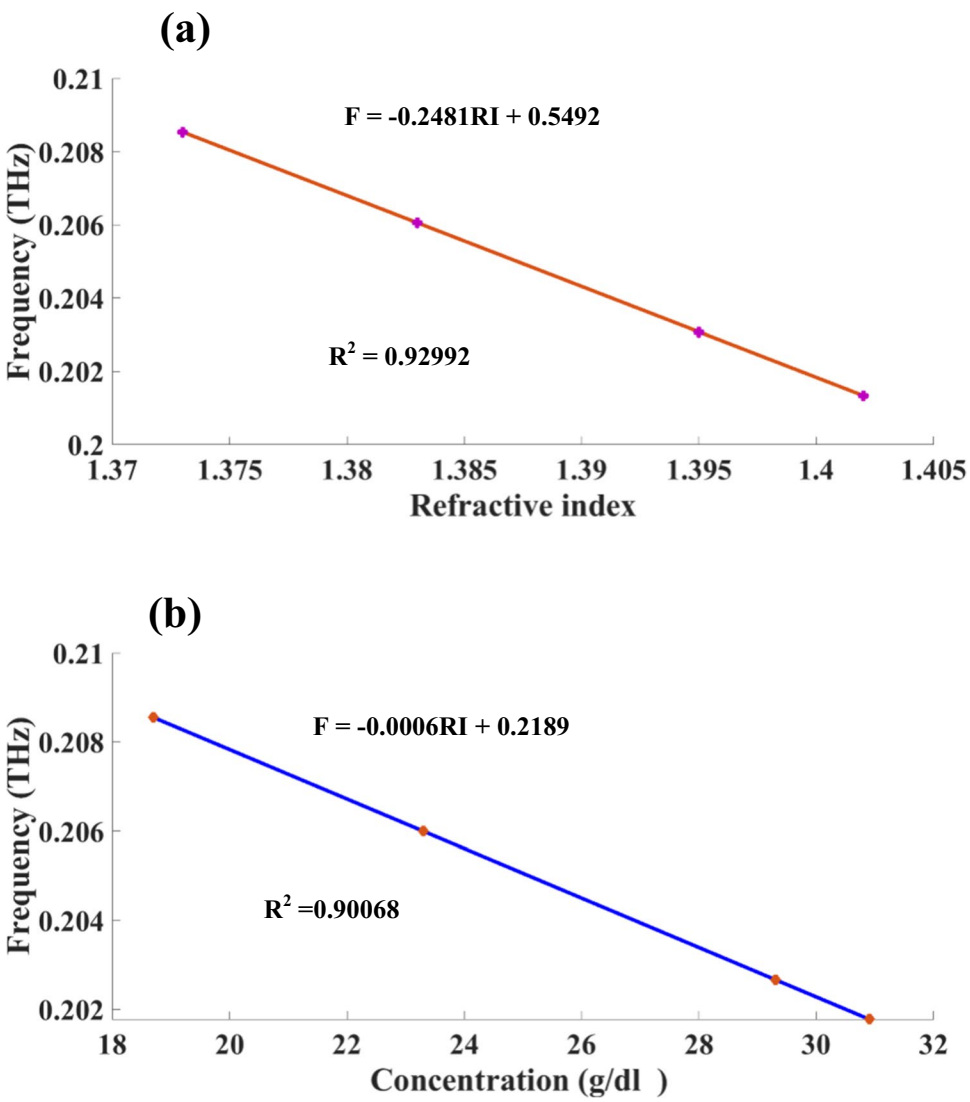

Fig. 8 presents the outcomes of the curve-fitting analysis, illustrating the association between resonance frequency and refractive as well as resonance frequency and the concentration of malaria samples

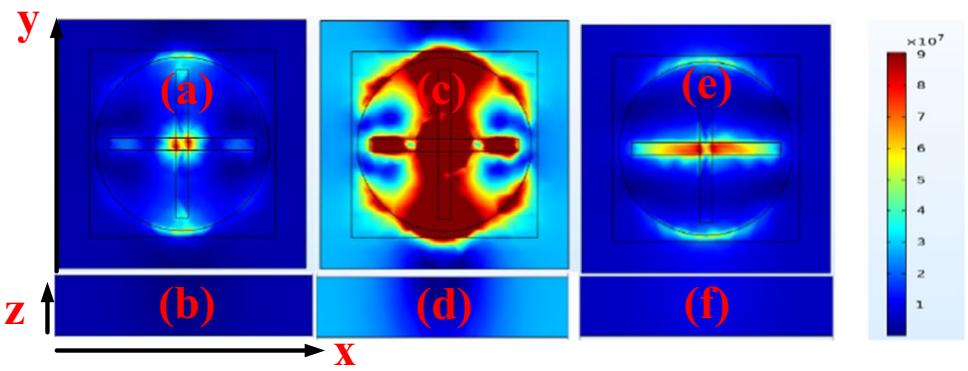

Fig. 9 illustrates the electric field distribution of the graphene-based sensor across three distinct frequencies: (a-b) 0.1 THz, (c-d) 0.25 THz, and (e–f) 0.3 THz

Table 1 Variation in Refractive Indices with Concentration Levels of Malaria Samples

Category	Healthy	Schizont	Ring	Trophozoite
n(RIU)	1.402	1.373	1.395	1.383
Conc.(g/L)	30.9	18.7	29.3	23.3

All resonator components are placed on a SiO_2 substrate, which provides mechanical support and stability. The substrate itself measures 10.75 µm in width and length, with a thickness of 1.58 µm. The height of the analyte is 1.5 µm (h).

Figure 1 shows various views of the sensor design being studied: (a) from above, (b) from the side, and (c) in three dimensions. The graphene layer is clearly visible on top of the substrate, illustrating its precise placement relative to the gold and silver components. The thickness of the graphene layer is specified as 0.34 nm [36–40]. The structure is designed to optimize the interaction of incident light with the surface plasmon resonances of each material layer. The top layer in this stack is graphene, which offers exceptional conductivity and facilitates the excitation of surface plasmons when light interacts with it. Beneath the graphene layer lies a thin film of gold, which supports and enhances the surface plasmon resonances. Gold's strong plasmonic response and ability to sustain localized surface plasmon resonances at specific frequencies are crucial for improving the sensor's sensitivity. The lowest layer in the stack is silver, which contributes additional plasmonic effects. Silver's unique properties complement those of gold, allowing for a broader range of resonance frequencies and enhancing the sensor's overall capabilities [41].

The refractive index of silicon dioxide is given by [42];

$$n(\lambda) = \sqrt{1 + \frac{B_1 C}{\lambda^2 - C_1} + \frac{B_2 \lambda^2}{\lambda^2 - C_2} + \frac{B_3 \lambda^2}{\lambda^2 - C_3}} \quad (1)$$

The dielectric constant of gold is determined by [43];

Table 2 Performance parameters of the proposed sensor

f(THz)	0.209	0.205	0.204	0.201
n(RIU)	1.373	1.383	1.395	1.402
df(THz)		0.004	0.001	0.003
dn(RIU)		0.01	0.012	0.007
S(GHzRIU^{-1})		400	83	429
FWHM(GHz)	39	39	39	39
FOM(RIU^{-1})		10.256	2.137	10.989
Q	5.359	5.256	5.231	5.154
DL		0.115	0.780	0.115
DR	1.058	1.038	1.033	1.018
SNR		0.103	0.026	0.077
SR		0.046	0.065	0.049
DA	25.641	25.641	25.641	25.641
X		0.002	0.001	0.001

$$\varepsilon_{Au} = \varepsilon_\infty - \frac{\omega_D^2}{\omega(\omega + j\gamma_D)} - \frac{\Delta_\varepsilon \Omega_L^2}{(\omega^2 - \Omega_L^2) + j\Gamma_L \omega} \quad (2)$$

Fabrication Feasibility

The process begins with the preparation of a silicon dioxide (SiO_2) substrate, which serves as the foundation for the sensor. The substrate is first cleaned thoroughly using standard semiconductor cleaning procedures, ensuring a clean and uniform surface. Next, a layer of silver (Ag) is deposited on the SiO_2 substrate using a thin-film deposition technique, such as physical vapor deposition (PVD) or chemical vapor deposition (CVD). This silver layer is then patterned into a square resonator with dimensions of 7.5 µm × 7.5 µm using photolithography and etching techniques.

Following the formation of the square resonator, a layer of gold (Au) is deposited over the substrate, covering the previously patterned square resonator. The gold layer is then patterned into two rectangular resonators, each measuring 3.72 µm in length and 0.5 µm in width, using

photolithography and etching processes. The next step involves the deposition of a graphene layer with a thickness of 0.34 nm on the substrate, covering the square and rectangular resonators. This graphene layer is then patterned into a circular resonator with a radius of 3.5 µm using photolithography and etching techniques. To complete the fabrication, the entire sensor structure, including the resonators and the substrate, is enclosed to protect it from environmental effects and ensure mechanical stability. Additionally, necessary electrical connections, such as electrodes or transmission lines, are integrated to enable the application of the terahertz frequency excitation and signal readout. Throughout the fabrication process, strict control over the dimensions, material properties, and alignment of the different resonator components is crucial to ensure the desired electromagnetic response and sensing performance of the device. Advanced characterization techniques, such as scanning electron microscopy (SEM), atomic force microscopy (AFM), and spectroscopic methods, are employed to verify the fabricated structure and its conformity to the design specifications.

When the sensor is exposed to a sample, such as a biological fluid containing malaria biomarkers (or other molecules associated with diseases), these molecules interact with the electromagnetic fields generated by the resonators. This interaction causes a shift in the resonance frequency of the sensor. For example, if a biomarker binds to the surface of the sensor, it changes the local refractive index, leading to a detectable shift in the frequency at which the sensor resonates. In a real-world application, this shift in resonance is detected and measured in real-time. The data from this measurement can then be processed using algorithms to determine whether specific biomarkers are present, and in

Table 3 The comparison between the suggested sensor and other cases

	S(GHz/RIU)	FOM(RIU^{-1})	D.L(RIU)	Q	Application
Ref [71]	23,000 nm/RIU	-	-	-	Malaria detection
Ref [72]	42,857.14 nm/RIU	47.44	0.007	-	Malaria detection
Ref [73]	33 GHz/RIU	-	-	-	THz sensing
Ref [74]	327 nm/ RIU	-	-	-	Detection of malaria
Ref [75]	240 GHz/RIU	-	-	-	Protein detection
Proposed sensor	429 GHz/RIU	2.137	0.115	5.359	Malaria Detection

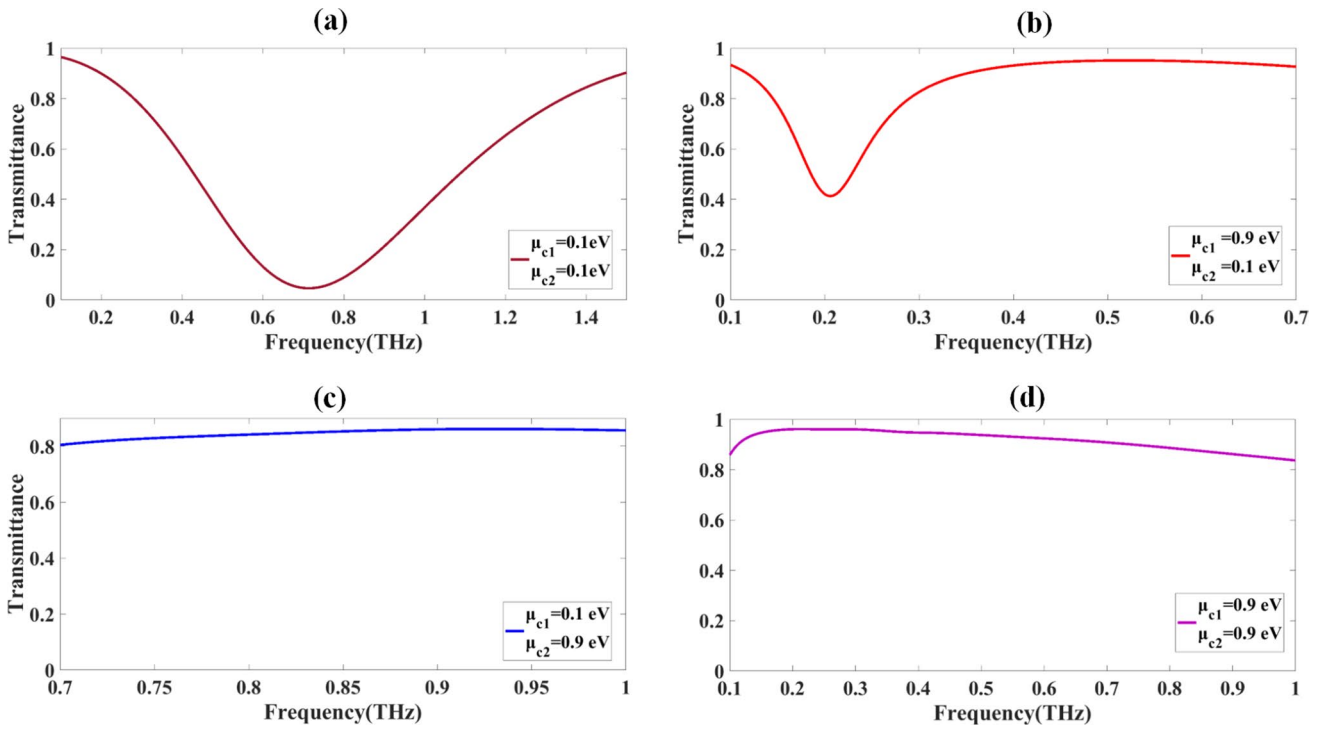

Fig. 10 demonstrates different transmittance cases of the proposed sensor design for encoding analysis

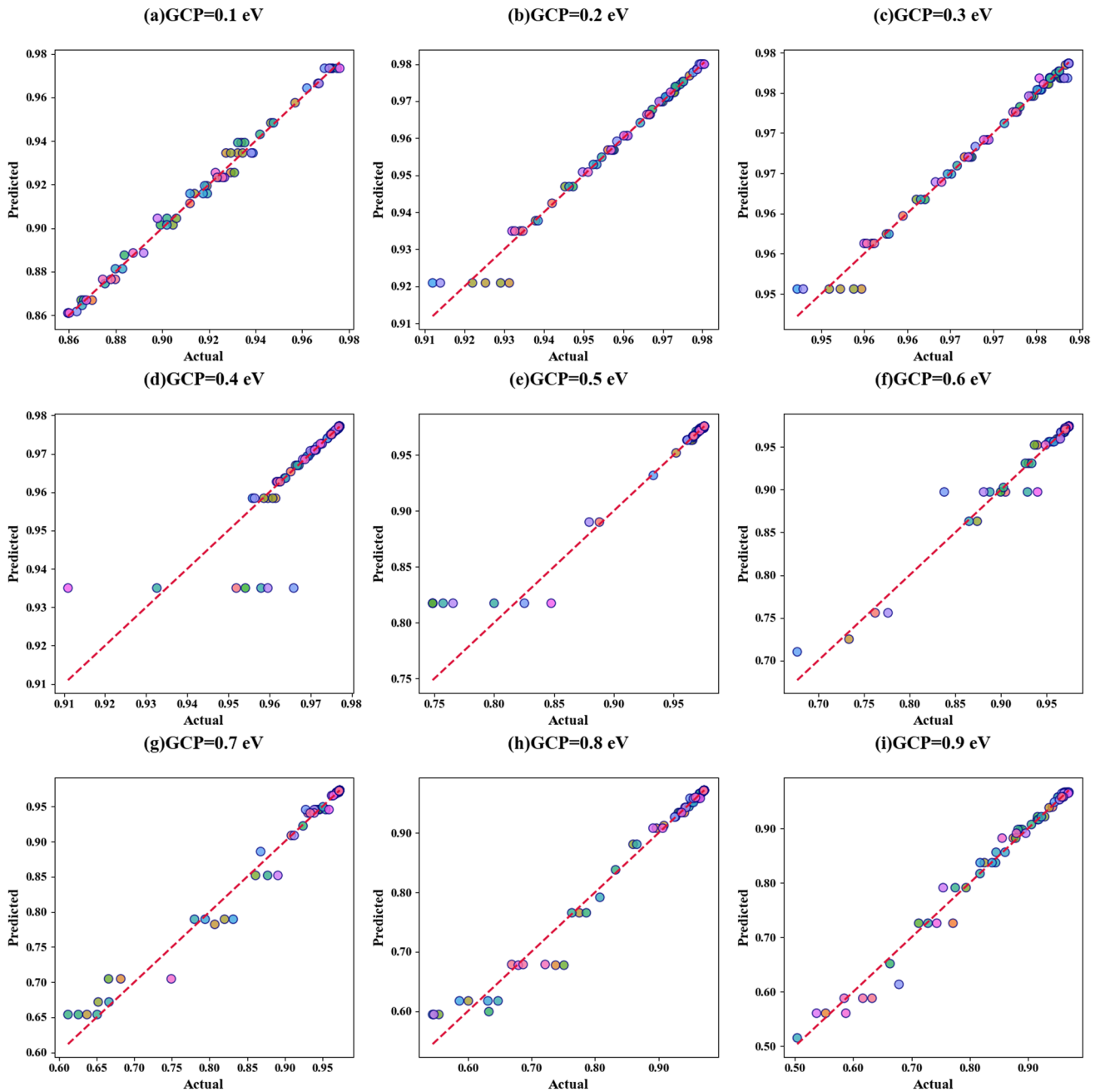

Fig. 11 illustrates scatter plots comparing the absorption values predicted by the XGR model with those obtained from simulations, focusing on the variation of GCP

what concentration. This makes the sensor a powerful tool for applications like early disease detection, where detecting small amounts of a particular biomarker can be crucial.

Graphene Conductivity Overview

A single sheet of carbon atoms in a hexagonal pattern, known as graphene, has captured significant scientific and technological interest due to its exceptional characteristics [44]. Its remarkable features include robustness, pliability, and superior electrical and heat conduction [45]. The distinctive qualities of graphene arise from its two-dimensional structure, where carbon atoms form sp^2 bonds [46]. This arrangement results in an incredibly thin yet extremely sturdy material, boasting strength roughly 200 times that of steel when comparing equal weights, while maintaining flexibility and low mass [47]. Graphene's electrical prowess is evident in its high electron mobility at ambient

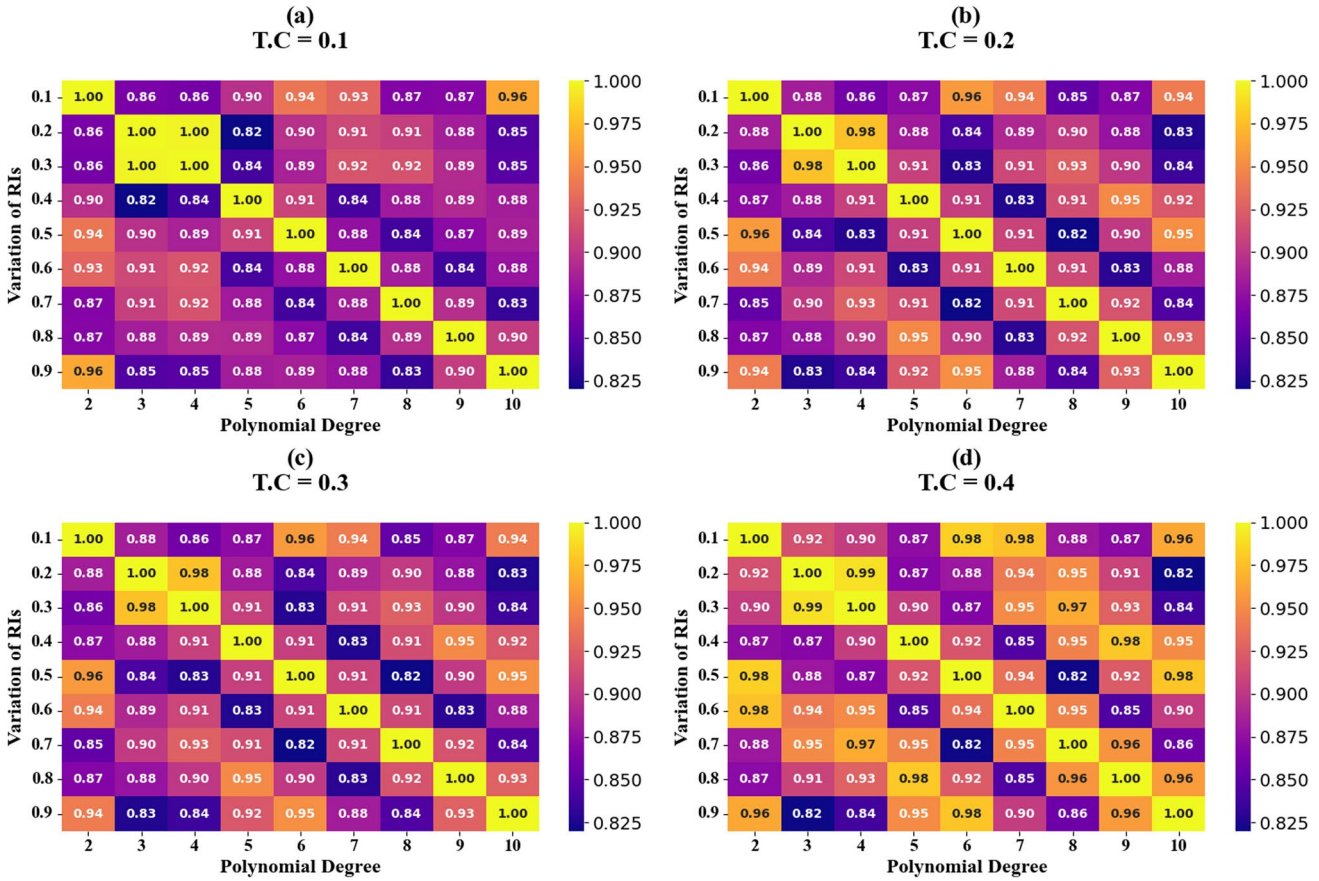

Fig. 12 displays heat map tables (HT) showing the R^2 scores of XGR models across different combinations of GCP

temperatures, making it ideal for various electronic uses [48]. Its conductivity can be enhanced through chemical alteration or structural modifications, opening doors for advanced transistors, see-through conductive layers, and detection devices [49].The material's thermal conductivity outperforms most known substances, positioning it as an excellent choice for heat dissipation in electronics and as a component in cutting-edge composite materials [50, 51].Apart from its electrical and mechanical attributes, graphene's transparency to light enables its use in clear electrodes for touch-sensitive displays, photovoltaic cells, and LEDs. Its ability to block gases and liquids also makes it valuable for protective coatings and filtration systems in water treatment and gas separation processes [52].Ongoing research continues to uncover graphene's potential in diverse areas such as energy storage, medical applications, and quantum computing. As production methods improve and new uses emerge, graphene remains at the forefront of technological advancement [53, 54].Graphene's unique electronic structure, particularly its linear dispersion relation near the Dirac points, leads to a finite but highly efficient electrical conductivity [55]. The Kubo formula allows researchers to quantitatively predict and analyze how external factors such as temperature, impurities, and substrate interactions influence graphene's conductivity. Eqs. 3–6 represednts the Kubo's formula [38].

$$\varepsilon(\omega) = 1 + \frac{\sigma_s}{\varepsilon_0 \omega \nabla} \tag{3}$$

$$\sigma_{intra} = \frac{-je^2 k_B T}{\pi \hbar^2 (w - j2\Gamma)} \left(\frac{\mu_c}{k_B T} + 2ln\left(e^{\frac{\mu_c}{k_B T}} + 1 \right) \right) \tag{4}$$

$$\sigma_{inter} = \frac{-je^2}{4\pi\hbar} ln\left(\frac{2|\mu_c| - (\omega - j2\Gamma)\hbar}{2|\mu_c| + (\omega - j2\Gamma)\hbar} \right) \tag{5}$$

$$\sigma_s = \sigma_{intra} + \sigma_{inter} \tag{6}$$

In this study, the selection of structural and material configurations was driven by the objective of optimizing sensor performance and functionality. The chosen structure was designed to enhance surface plasmon resonance (SPR). The arrangement of materials—graphene, gold (Au), and silver (Ag)—was engineered to exploit their complementary properties. Graphene provides exceptional electrical

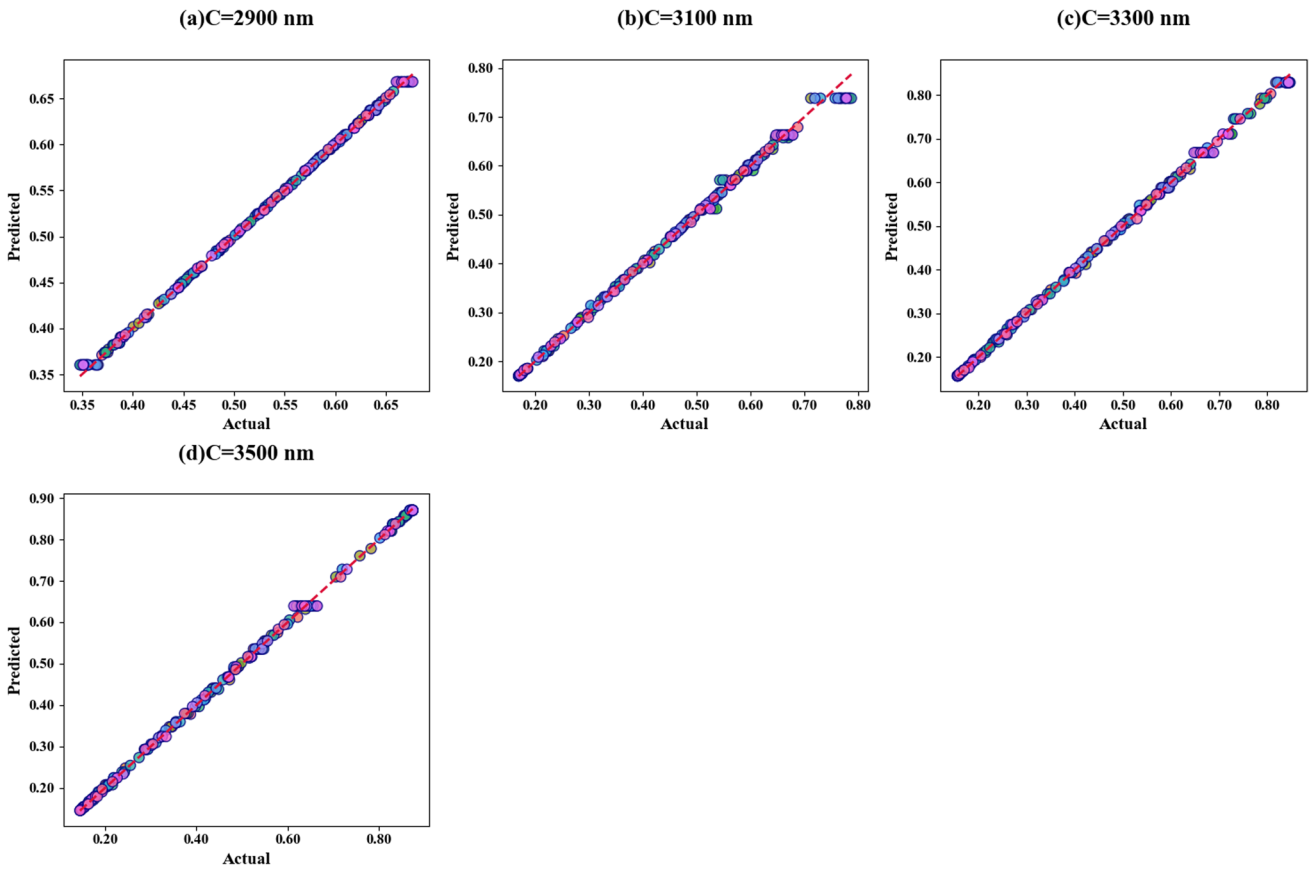

Fig. 13 illustrates scatter plots comparing the absorption values predicted by the XGR model with those obtained from simulations, focusing on the variation of C (dimensions of circular resonator)

conductivity and a high surface-to-volume ratio, facilitating efficient excitation of surface plasmons. Gold and silver were incorporated due to their strong plasmonic responses and their ability to support localized surface plasmon resonances at varying frequencies. The layering of these materials is intended to maximize the interaction between incident light and surface plasmons, thereby enhancing sensor sensitivity. Surface plasmons, which are collective oscillations of free electrons at the interface between a metal and a dielectric material, are excited by incident light and propagate along the metal layers in the proposed structure. The arrangement of graphene, gold, and silver is designed to optimize this propagation and concentration. The unique combination and sequence of these materials create specific conditions that amplify plasmonic effects, thus improving the sensor's ability to detect minute changes in the refractive index of the surrounding medium. For manuscripts focused solely on simulations, it is essential to highlight the novelty and significance of the proposed structure. The emphasis should not only be on presenting simulation results but also on elucidating how the selected structure and material arrangement contribute to the overall performance and efficacy of the sensor. By detailing the rationale behind these choices and their impact on surface plasmon behaviour, the innovative aspects of the design and its potential advantages over existing technologies can be effectively demonstrated.

The Principle of Malaria Detection Based on RIs

The application of refractive indices in malaria detection capitalizes on the principle that variations in the optical properties of a medium can signify the presence of specific biological entities. This diagnostic approach involves evaluating changes in the refractive index of a biological sample, such as blood, in response to malaria parasites. Malaria detection via refractive index measurement relies on the fact that the presence of Plasmodium species alters the refractive index of infected blood. This alteration is attributed to the density and refractive characteristics of the parasitized red blood cells, which modify the optical properties of the blood. Refractive index-based sensing techniques can detect these modifications, allowing for the identification of malaria infection with high sensitivity and specificity. Refractive index-based detection offers notable advantages, including non-invasive measurement capabilities and potential for real-time monitoring. Techniques

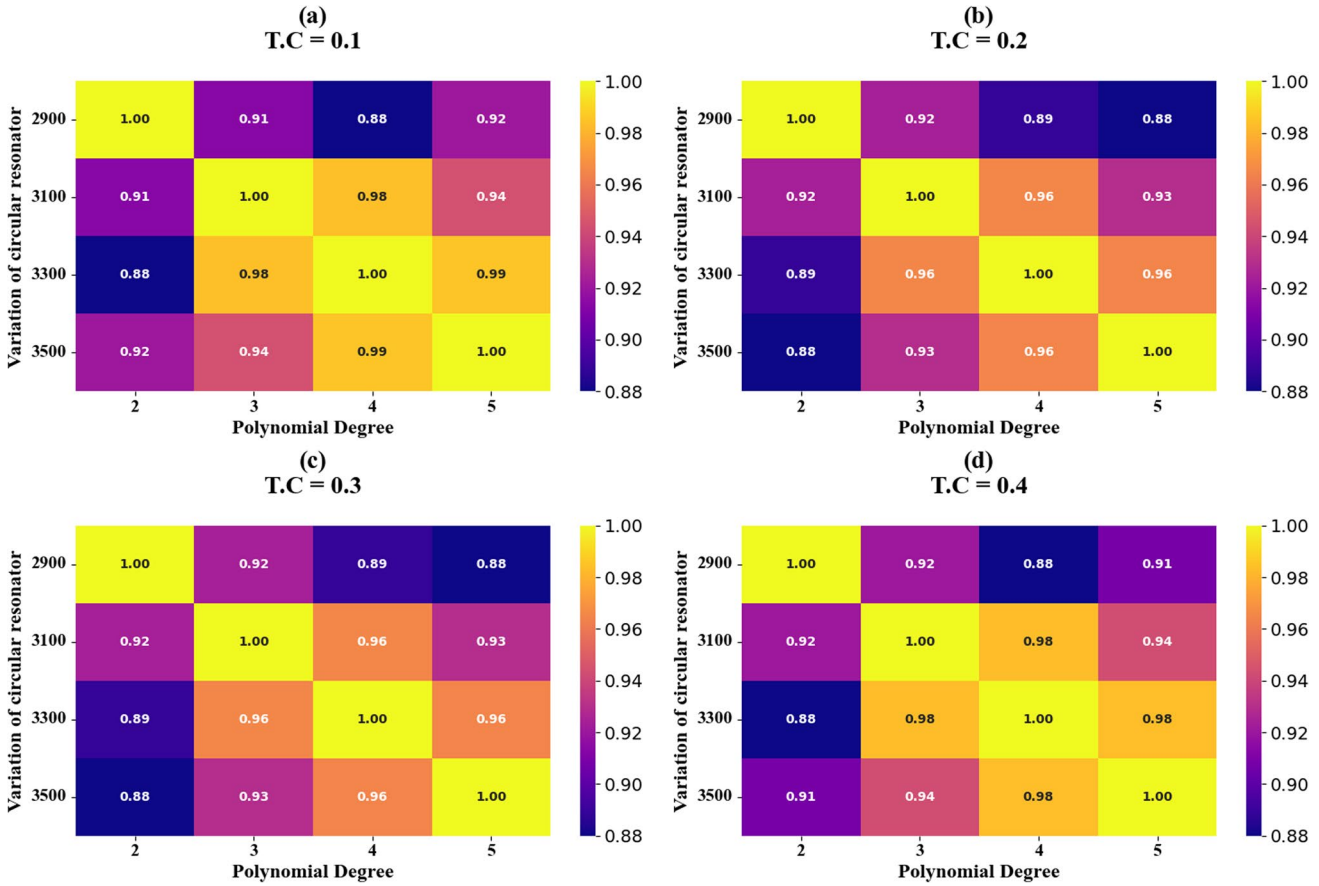

Fig. 14 displays HT showing the R^2 scores of XGR models across different combinations of C

such as optical coherence tomography (OCT), refractometry, and surface plasmon resonance (SPR) are employed to detect refractive index changes induced by malaria [56–62].These techniques can be integrated into diagnostic devices, facilitating rapid and precise malaria detection, particularly in regions where conventional diagnostic methods are less accessible.

Results and Discussion

The model depicted in Fig. 1 underwent comprehensive simulation employing COMSOL Multiphysics version 6.2. The simulation leveraged the finite element method (FEM) to discretize the model geometry into a mesh of smaller, simpler elements. This discretization process employed Delaunay tessellation, an algorithm that generates a mesh composed of well-shaped triangles (in 2D) or tetrahedra (in 3D), ensuring optimal element quality and minimizing numerical errors [63, 64].To accurately represent the periodic nature of the model's structure, periodic boundary conditions were applied. These conditions enforce continuity of the solution variables across opposite boundaries, effectively simulating an infinite array of the modeled unit cell. This approach significantly reduces computational overhead by allowing the simulation of a representative unit rather than the entire, potentially vast, structure [65].The simulation is tailored to address the specific requirements of malaria detection, taking into account the electromagnetic properties of the materials involved and the interaction of incident light with the periodic nanostructures. The wavelength-dependent refractive indices of the substrate, nanoparticles, and surrounding medium were incorporated to accurately model the plasmonic resonance phenomena that underpin the detection mechanism [66].In this paper, we have conducted a rigorous analysis of malaria samples across a spectrum of concentrations. The samples were prepared at concentrations of 30.9 g/dl (n = 1.402), 29.3 g/dl (n = 1.395), 23.3 g/dl (n = 1.383), and 18.7 g/dl (n = 1.373), where 'n' represents the refractive index at a reference wavelength [67] Fig. 2.

Optimization of Graphene Chemical Potential (GCP)

Initially, we examined the impact of varying GCP on the transmittance response of the proposed sensor design.

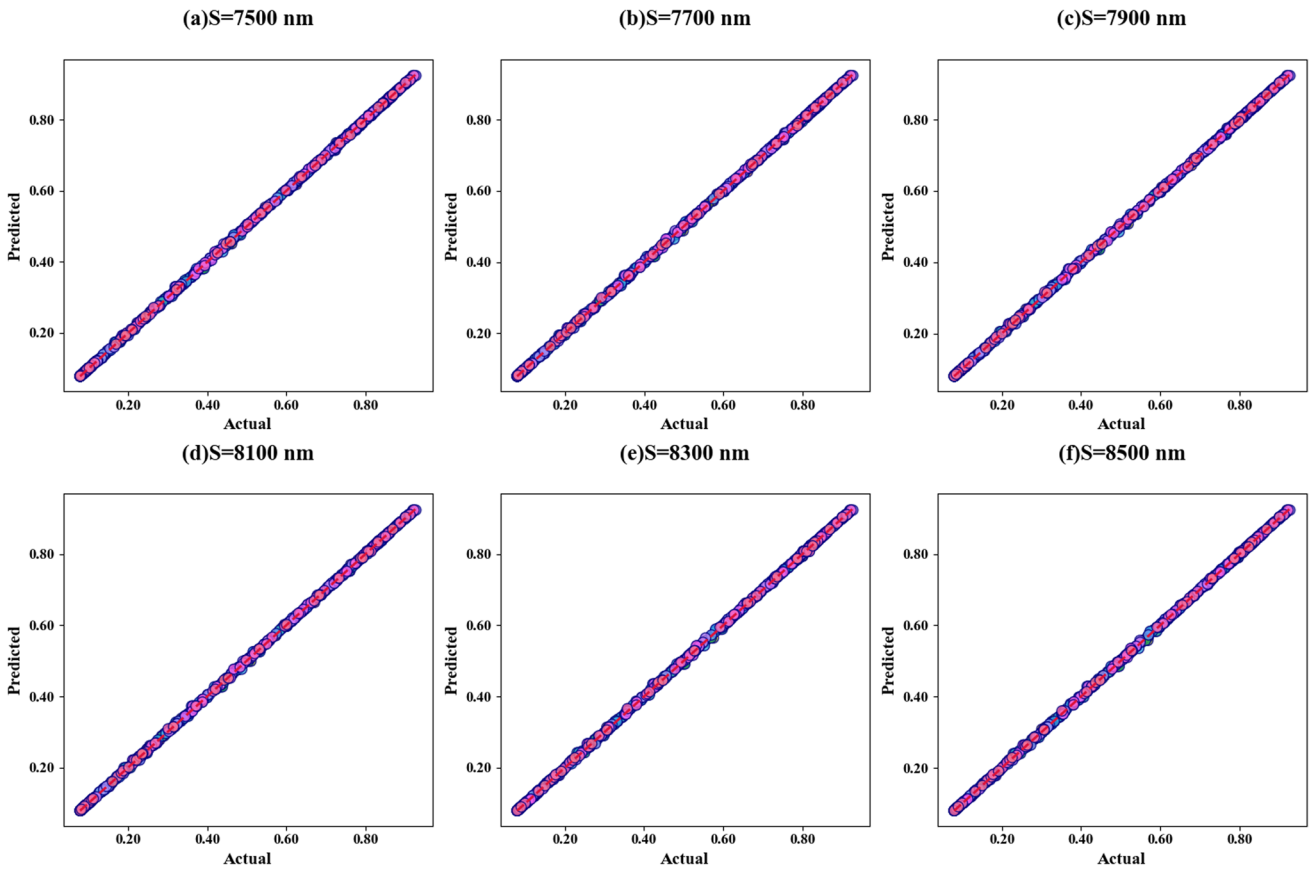

Fig. 15 illustrates scatter plots comparing the absorption values predicted by the XGR model with those obtained from simulations, focusing on the variation of S (dimensions of square resonator)

Figure 3a and b depicts how these variations influence the transmittance characteristics of the sensor.

The GCP quantifies the energy gap between graphene's Fermi level and its Dirac point, which significantly affects its electrical behaviour. Figure 3a presents a plot showing how transmittance varies with different GCP values, ranging from 0.1 eV to 0.9 eV in 0.1 eV increments. The plots demonstrate a consistent inverse correlation between transmittance and the graphene chemical potential (GCP). Figure 3b provides a color-coded spectral representation of transmittance behaviour across the spectrum. The spectral analysis indicates that as GCP values increase, there is a noticeable shift toward higher attenuation of transmittance. Notably, for lower GCP values, explicitly between 0.1 eV and 0.3 eV, there are no significant reductions in transmittance, suggesting that within this range, changes in GCP have a minimal impact on the sensor's optical properties. In contrast, for GCP values exceeding 0.3 eV, substantial and significant drops in transmittance become evident across the 0.1–0.3 THz frequency band. The observed transmittance reductions are pronounced, with values of 85.96%, 90.99%, 94.65%, 87.03%, 74.85%, 67.67%, 60.78%, 54.39%, and 48.61%. The colour plot in Fig. 3b demonstrates a clear leftward shift in transmittance response with increase in GCP. Variations in GCP induce changes in transmittance by altering the interactions within graphene's electronic and optical properties. Adjustments to the GCP directly affect the Fermi level's position relative to the Dirac point within graphene's electronic structure. This repositioning of the Fermi level has a profound impact on both the electronic and optical properties of the material. An increase in GCP shifts the Fermi level away from the Dirac point, potentially placing it within either the conduction or valence band, depending on the polarity of the GCP. This shift modifies the carrier concentration in graphene, typically resulting in a higher density of carriers corresponding to the increased GCP. Changes in carrier concentration subsequently affect the optical conductivity of graphene, which generally increases with rising carrier density. Additionally, the phenomenon of Pauli blocking, which becomes more pronounced at higher carrier concentrations, restricts certain electronic transitions, particularly those occurring below twice the Fermi energy. Furthermore, fluctuations in carrier concentration can influence the generation of plasmons in graphene, thereby significantly affecting its optical properties, especially in the terahertz frequency range.

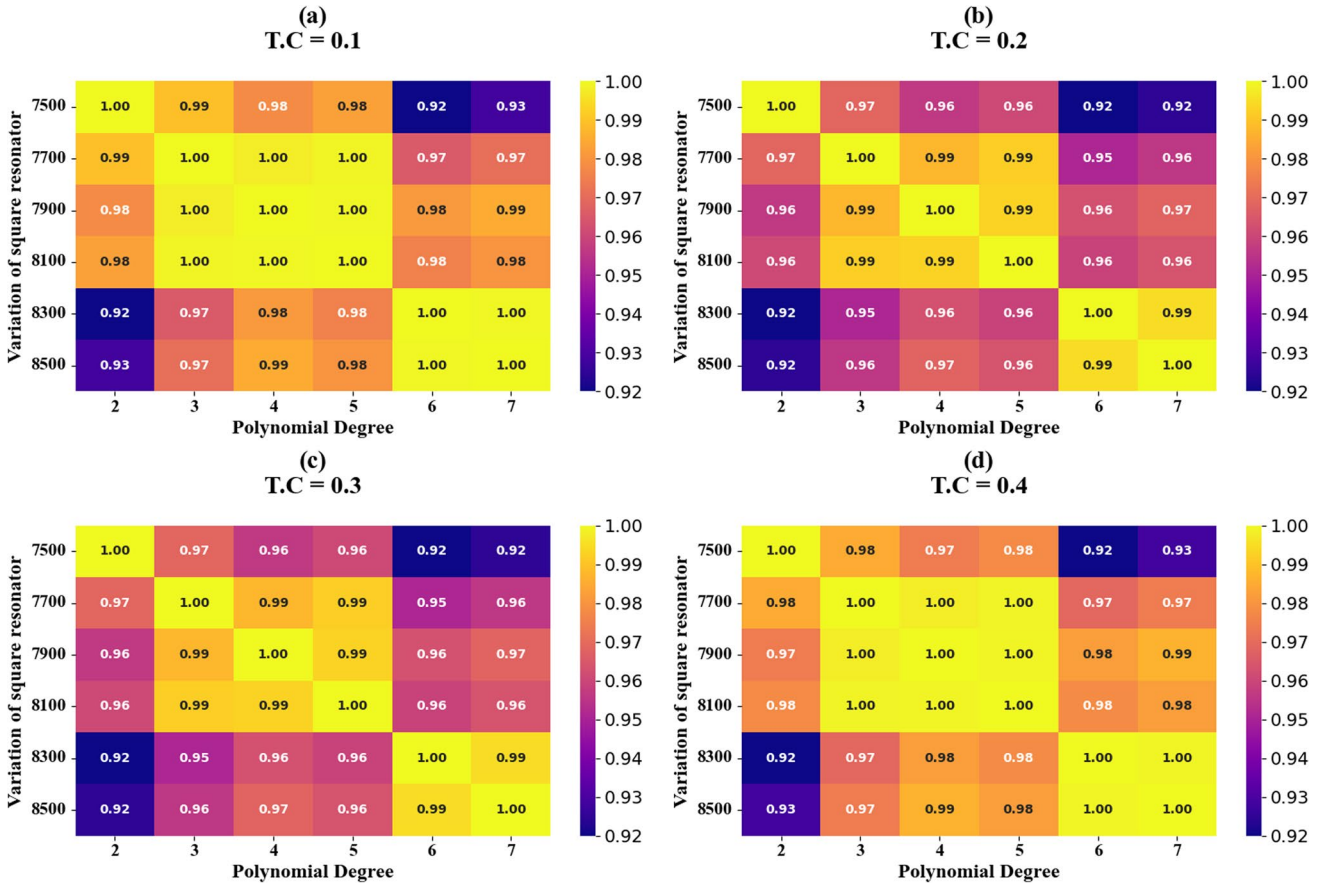

Fig. 16 displays HT showing the R^2 scores of XGR models across different combinations of S

Optimization of Parameters

Subsequently, we investigated the potential for tuning by varying resonator parameters. The outcomes of this investigation are presented in Figs. 3–4. Figures 5a and billustrate the effects of modifications to the circular resonator on the transmittance response of the sensor design.

The diameter of the circular resonator was varied within the range of 2900 nm to 3500 nm, and the corresponding results are depicted in Fig. 4a and b. Figure 4a presents the transmittance spectrum corresponding to frequencies between 1.1 THz and 1.7 THz. The results demonstrate marked reductions in transmittance at specific diameters: 34.75% at 2900 nm, 16.97% at 3100 nm, 15.62% at 3300 nm, and 14.44% at 3500 nm. These reductions occur at frequencies of 1.70 THz, 1.53 THz, 1.476 THz, and 1.42 THz, respectively. Figure 4b provides a color-coded representation of the transmittance spectral response as a function of frequency and the various circular resonator diameters, clearly illustrating how the transmittance response shifts with increasing diameter. Notably, a discernible leftward shift in the transmittance response is observed with each increment in the resonator diameter. In the second case, we investigated the impact of varying the width of two rectangular resonators on the transmittance response and the results are demonstrated in Figs. 4and b. The widths of the resonators were adjusted from 1000 to 5000 nm in 500 nm increments. The transmittance spectra exhibit significant changes within the frequency range of 0.2 THz to 2 THz. Figure 4c shows the transmittance drops at various frequencies resulting from these width adjustments: 6.22%, 6.99%, 8.24%, 10.13%, 12.58%, 13.87%, 9.44%, 8.86%, and 7.87%. Figure 4d, leveraging a Fermi plot, further demonstrates that the transmittance response shifts toward lower frequencies as the widths of the rectangular resonators increase. In the third case, we analysed the effect of varying the height of rectangular resonators on transmittance, with results presented in Figs. 4e and f. The height of the resonators was varied from 100 to 900 nm in 100 nm increments across 0.5 THz to 2 THz. Figure 4e, a line plot, displays specific transmittance decreases at various frequencies as resonator height changes: 5.89%, 6.52%, 7.75%, 9.03%, and 11.00%, occurring at frequencies of 1.759 THz, 1.89 THz, 1.895 THz, 1.908 THz, and 1.865 THz, respectively. Figure 4f, a Fermi plot, indicates the same results.

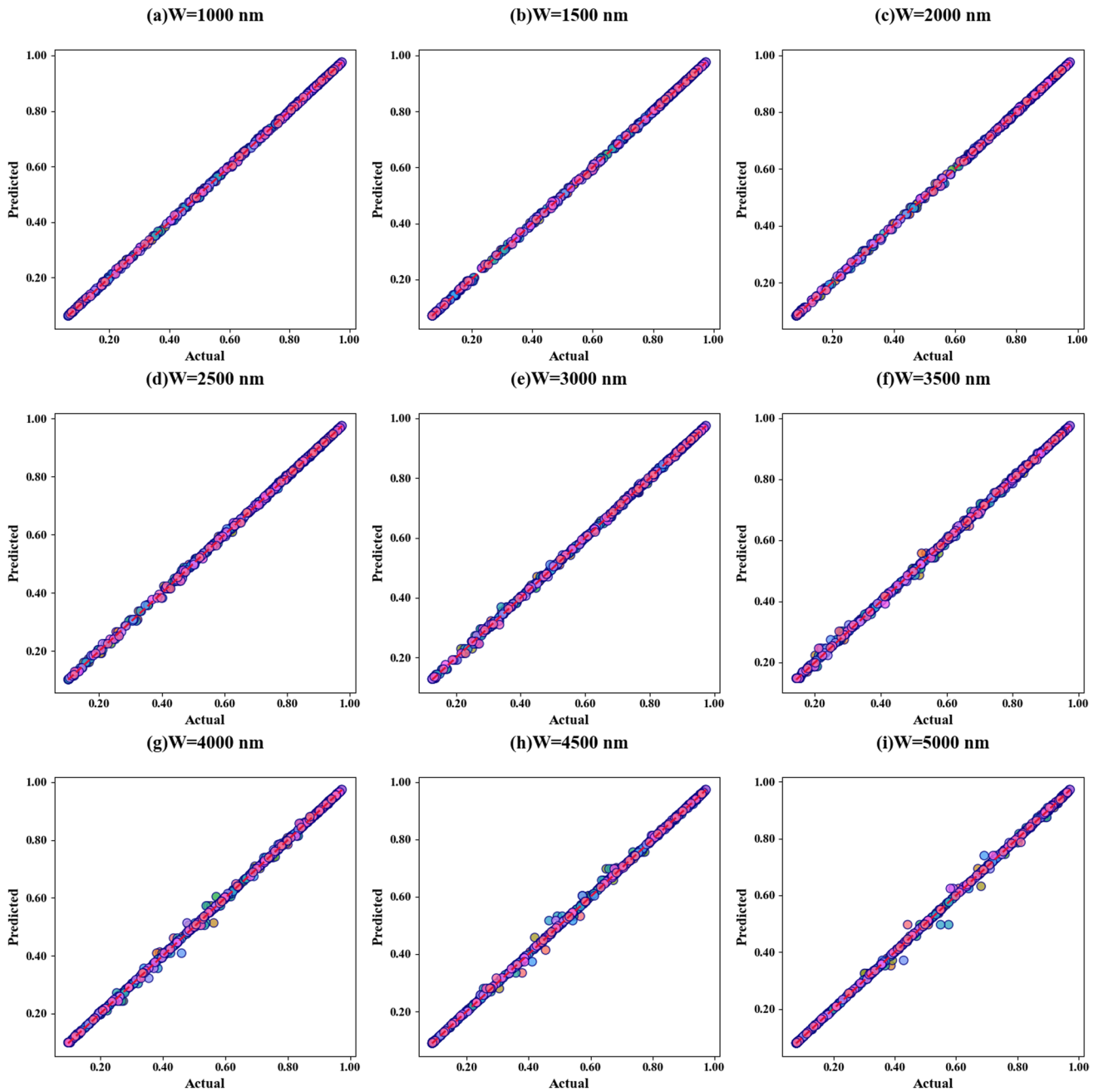

Fig. 17 illustrates scatter plots comparing the absorption values predicted by the XGR model with those obtained from simulations, focusing on the variation of W (width of rectangular resonators)

Our fourth study investigated the impact of varying the size of square resonators on transmittance, as illustrated in Figs. 6a and 6b. Figure 6a presents variations in resonator size from 7500 to 8500 nm, with increments of 200 nm. We recorded transmittance decreases of 7.75%, 7.90%, 7.97%, 7.92%, 7.95%, and 7.98% at frequencies of 1.894 THz, 1.88 THz, 1.872 THz, 1.877 THz, 1.858 THz, and 1.859 THz, respectively. The Fermi plot shown in Fig. 6b confirms that the transmittance response increases with an increase in the size of the square resonator, accompanied by a broadening of the transmittance band. In the final investigation of parameter optimization, we assessed the effect of the angle of incidence on transmittance, as depicted in Figs. 6c and 6d. The incident angle was varied from 0° to 80° in 10° increments, and its influence on transmittance was evaluated over a simulated frequency range of 0.1 THz to 0.5 THz. Figure 6c illustrates the specific transmittance reductions at different frequencies due to changes in the angle of incidence. The

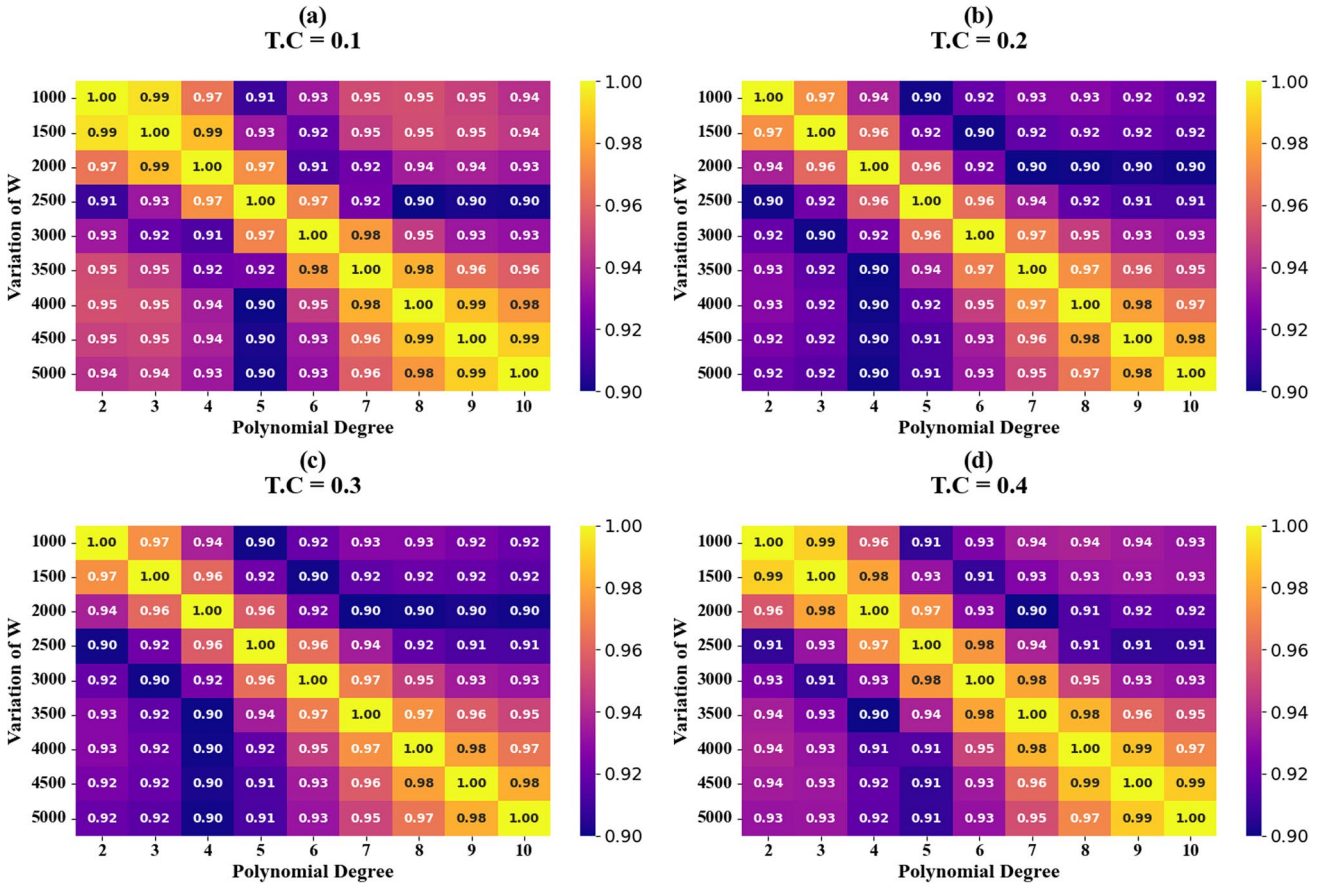

Fig. 18 displays HT showing the R^2 scores of XGR models across different combinations of W

recorded transmittance drops of 83.98%, 83.78%, 83.17%, 82.05%, 80.26%, 77.45%, 72.90%, 64.95%, and 48.61% are attained across the 0.1 THz to 0.3 THz frequency range. Transmittance variations that arises due to parameter optimization, primarily result from changes in the resonator's interaction with electromagnetic waves. Adjustments to these parameters can shift the resonant frequency of the system, which impacts the coupling efficiency between the resonator and incident electromagnetic waves, thereby reducing energy transmission at specific frequencies. Additionally, such modifications can induce impedance mismatches between the resonator and its surrounding medium, leading to increased reflection or absorption of electromagnetic waves and consequently diminished transmittance. Changes in resonator parameters also affect the spatial distribution and intensity of localized electromagnetic fields, potentially enhancing wave confinement within the resonator and reducing transmitted energy. Furthermore, alterations in resonator dimensions or material properties can modify the effective characteristics of the material, such as permittivity and permeability, resulting in increased material losses and greater energy dissipation, which further reduces transmittance. In certain cases, parameter adjustments may also induce destructive interference among different modes or structural components, contributing to a decrease in overall transmittance.

Detection Analysis

Upon optimizing the sensor design, it was utilized for malaria detection. Figure 7 demonstrates the impact of refractive index (RI) variations on transmittance responses, highlighting the significant dips observed. The observed drops in transmittance are 48.26%, 48.12%, 47.99%, and 47.93% at frequencies of 0.209 THz, 0.205 THz, 0.204 THz, and 0.201 THz, respectively. These transmittance reductions are associated with RI changes ranging from 1.373 to 1.402.

Figures 8a and 8b demonstrates a comprehensive curve-fitting analyses depicting the correlations between resonance frequency and two key parameters: refractive index (RI) and concentration. Figure 8a exemplifies a linear regression model correlating resonance frequency with RI, demonstrating an inverse relationship with transmittance. These linear fit yields a coefficient of determination (R^2)

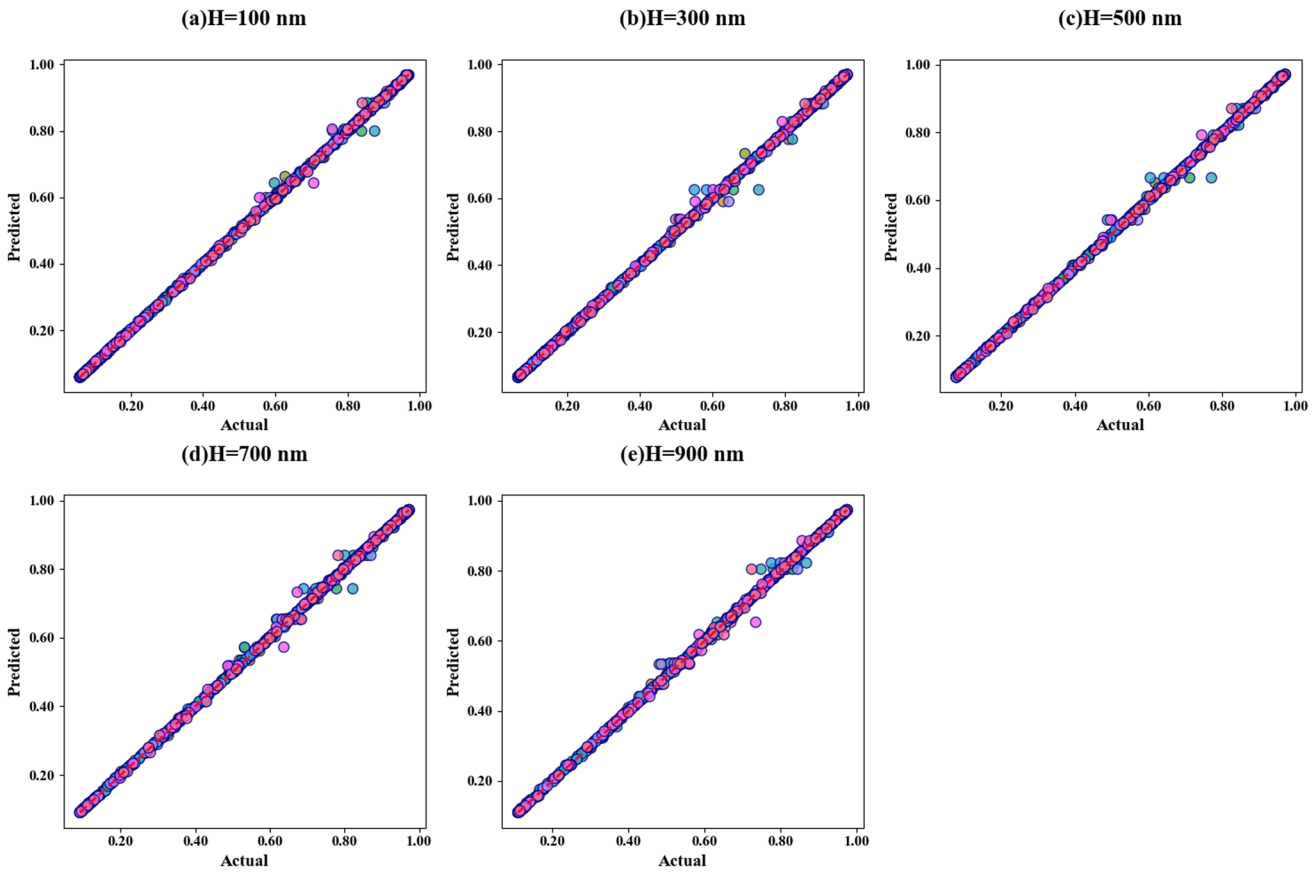

Fig. 19 illustrates scatter plots comparing the absorption values predicted by the XGR model with those obtained from simulations, focusing on the variation of H (height of rectangular resonators)

of 92.99% indicating a strong goodness of fit. Analogously, Fig. 6b employs a linear regression approach to relate resonance frequency to concentration, similarly exhibiting an inverse relationship with transmittance. This model achieves a robust R^2 value of 90.068%.

The derived linear equations for these relationships are as follows:

For resonance frequency vs. RI

$$F = -0.2481RI \times 0.5492 \tag{7}$$

For resonance frequency vs. concentration

$$F = -0.0006RI \times 0.2189 \tag{8}$$

Electric Field Analysis

Figure 9 illustrates the electric field distributions for the proposed metasurface design at three distinct frequencies. At 0.1 THz, the electric field is uniformly distributed with minimal localization or scattering on the metasurface, indicating low electromagnetic energy absorption and high transmittance Table 1.

At 0.25 THz, there is a significant increase in absorption along with pronounced scattering of the electric field across the metasurface. This behaviour reflects a more effective interaction between the metasurface and the incident electromagnetic waves, leading to enhanced absorption capabilities. The increased scattering at this frequency suggests a more substantial interaction between the electric field and the metasurface, resulting in greater energy absorption. In contrast, at 0.3 THz, the electric field distribution is similar to that observed at 0.1 THz, indicating comparable characteristics of minimal absorption and high transmittance through the material.

The efficacy of any sensor is determined by various metrics. Some of these metrics include [68]:

$$S = \frac{\Delta f}{\Delta n} \tag{9}$$

$$FOM = \frac{S}{FWHM} \tag{10}$$

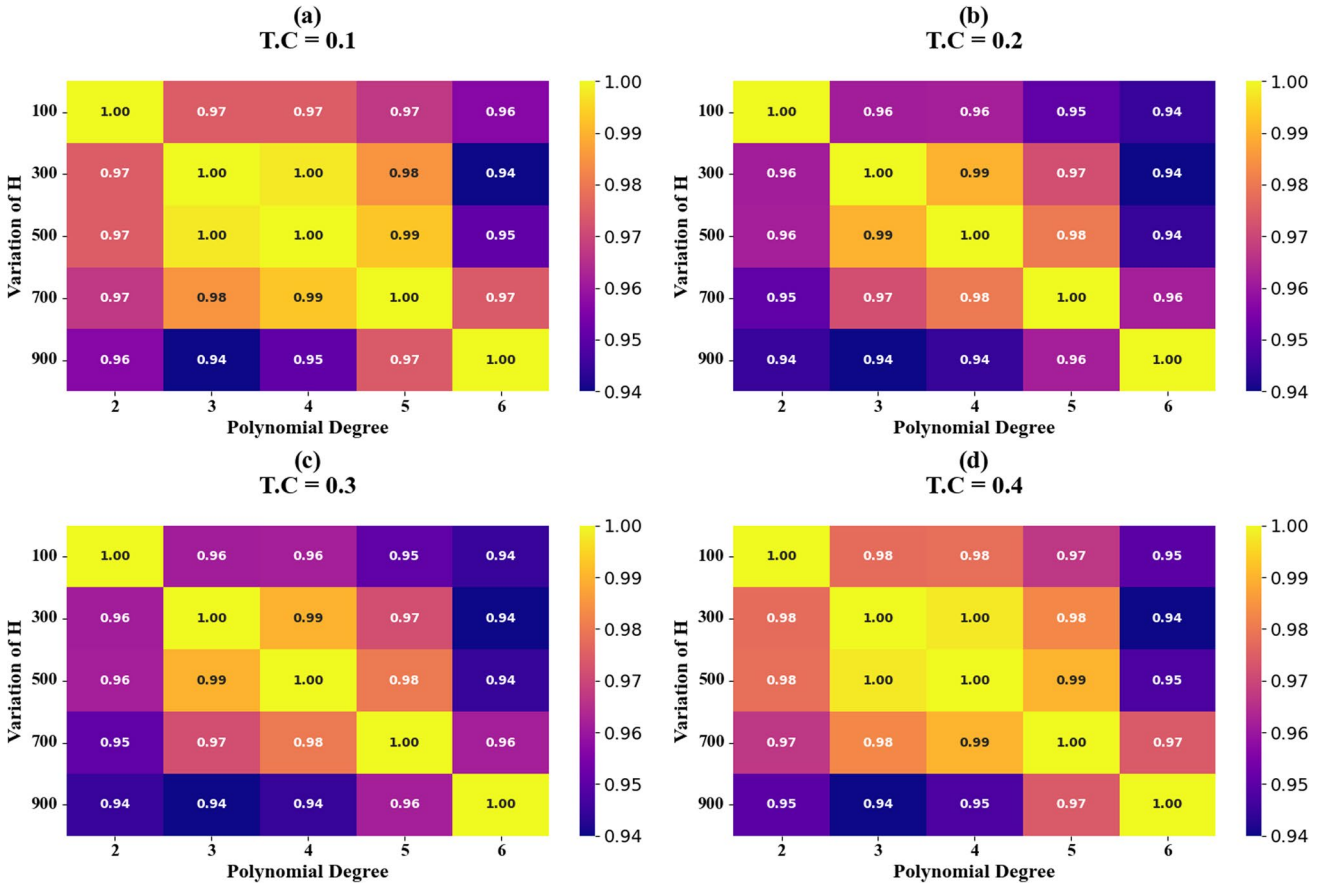

Fig. 20 displays HT showing the R^2 scores of XGR models across different combinations of H

$$Q = \frac{fr}{FWHM} \tag{11}$$

$$DL = \left(\frac{\Delta n}{1.5}\right) \times \left(\frac{FWHM}{\Delta f}\right)^{1.25} \tag{12}$$

$$DR = \frac{f_r}{\sqrt{FWHM}} \tag{13}$$

$$SNR = \frac{\Delta f}{FWHM} \tag{14}$$

$$SR = S \times DL \tag{15}$$

$$DA = \frac{1}{FWHM} \tag{16}$$

where symbols retains their definitions as given by[69, 70].

Table 2 summarizes the performance parameters of the proposed malaria detection sensor. The sensor operates within defined frequencies and detects malaria samples with refractive indices ranging from 1.373 to 1.402 RIU. Sensitivity varies from 83 to 429 GHz RIU^{-1} indicating the sensor's response to refractive index changes. The spectral resolution, measured as full width at half maximum (FWHM), is consistently 39 GHz. Figure of merit (FOM) values range from 2.137 to 10.989 RIU^{-1}, reflecting the sensor's effectiveness in detecting malaria-related refractive index changes. Key parameters include the quality factor (Q), which ranges from 5.154 to 5.359. Detection limits (DL), representing the minimum detectable concentration, range from 0.115 to 0.780. The dynamic range (DR) of detectable signal levels spans from 1.018 to 1.058. The signal-to-noise ratio (SNR), crucial for signal clarity, varies from 0.026 to 0.103. Sensor resolution (SR), which reflects the ability to distinguish closely spaced signals, ranges from 0.046 to 0.065. Measurement uncertainty (X) is minimal, between 0.001 and 0.002, indicating high precision. Detection accuracy (DA) remains constant at 25.641, demonstrating the sensor's reliable measurement of refractive indices. These parameters collectively characterize the sensor's operational capabilities and performance. Table 3 provides a comparative analysis of the proposed sensor with similar works. This comparison

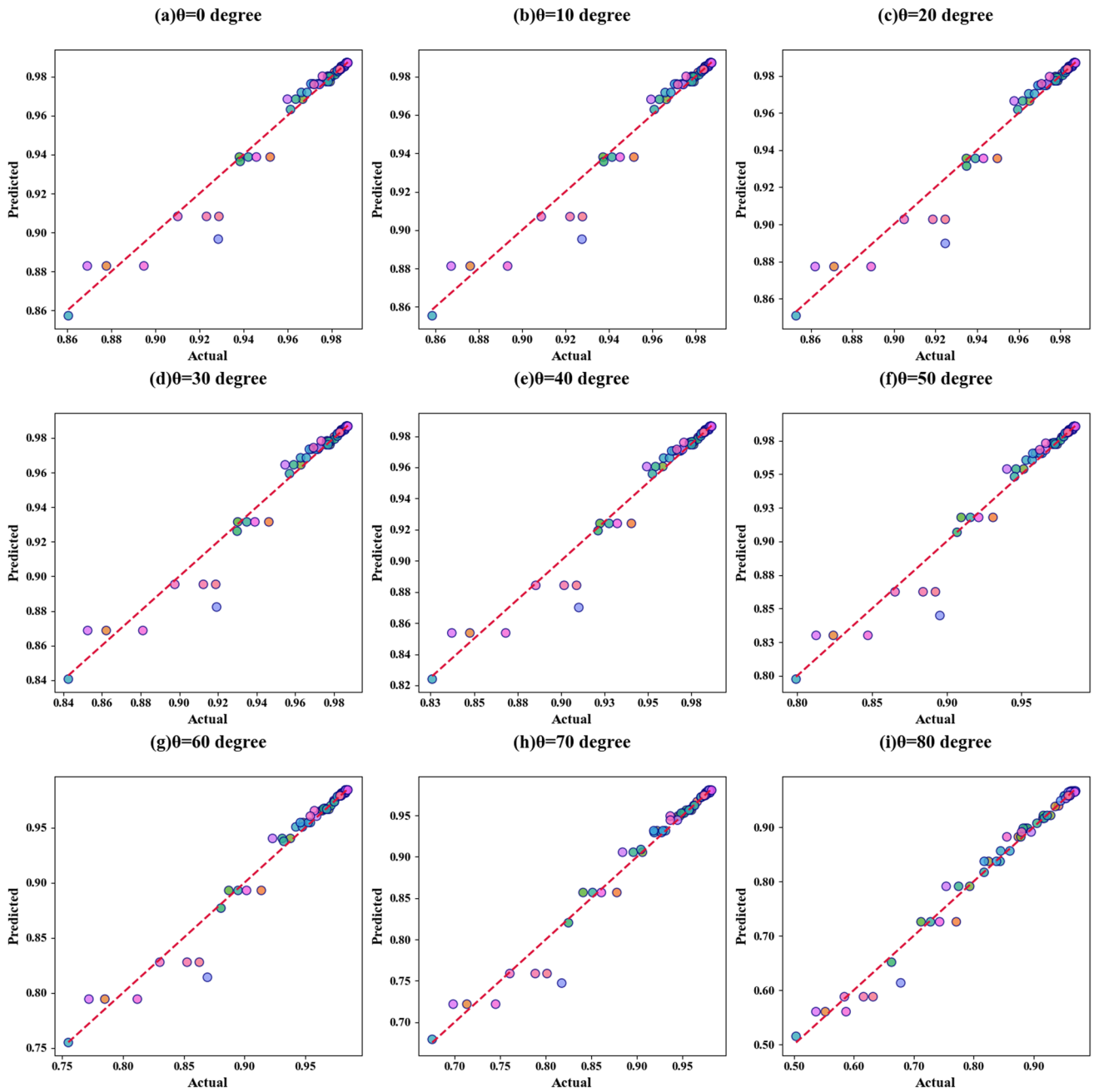

Fig. 21 illustrates scatter plots comparing the absorption values predicted by the XGR model with those obtained from simulations, focusing on the variation of θ (The angle of incidence)

demonstrates the proficiency of the proposed sensor in comparison to other cases in literature.

Encoding

Figure 10 illustrates the encoding applications of the sensor, as represented by different scenarios across various resonator geometries. In scenario 10a, parameter μ_{c1} is applied to both the plus-shaped and circular resonators, whereas μ_{c2} is applied to the square resonator. In scenario 10b, μ_{c1} is applied to the square resonator, and μ_{c2} is applied to the plus-shaped and circular resonators. Scenario 10c shows μ_{c1} applied uniformly across all resonators, while in scenario 10d, μ_{c2} is applied uniformly across all resonators. In Figs. 10, the graphs demonstrate minimal transmission. Conversely, Figs. 8 demonstrate near-complete transmission across the entire frequency spectrum. High transmittance

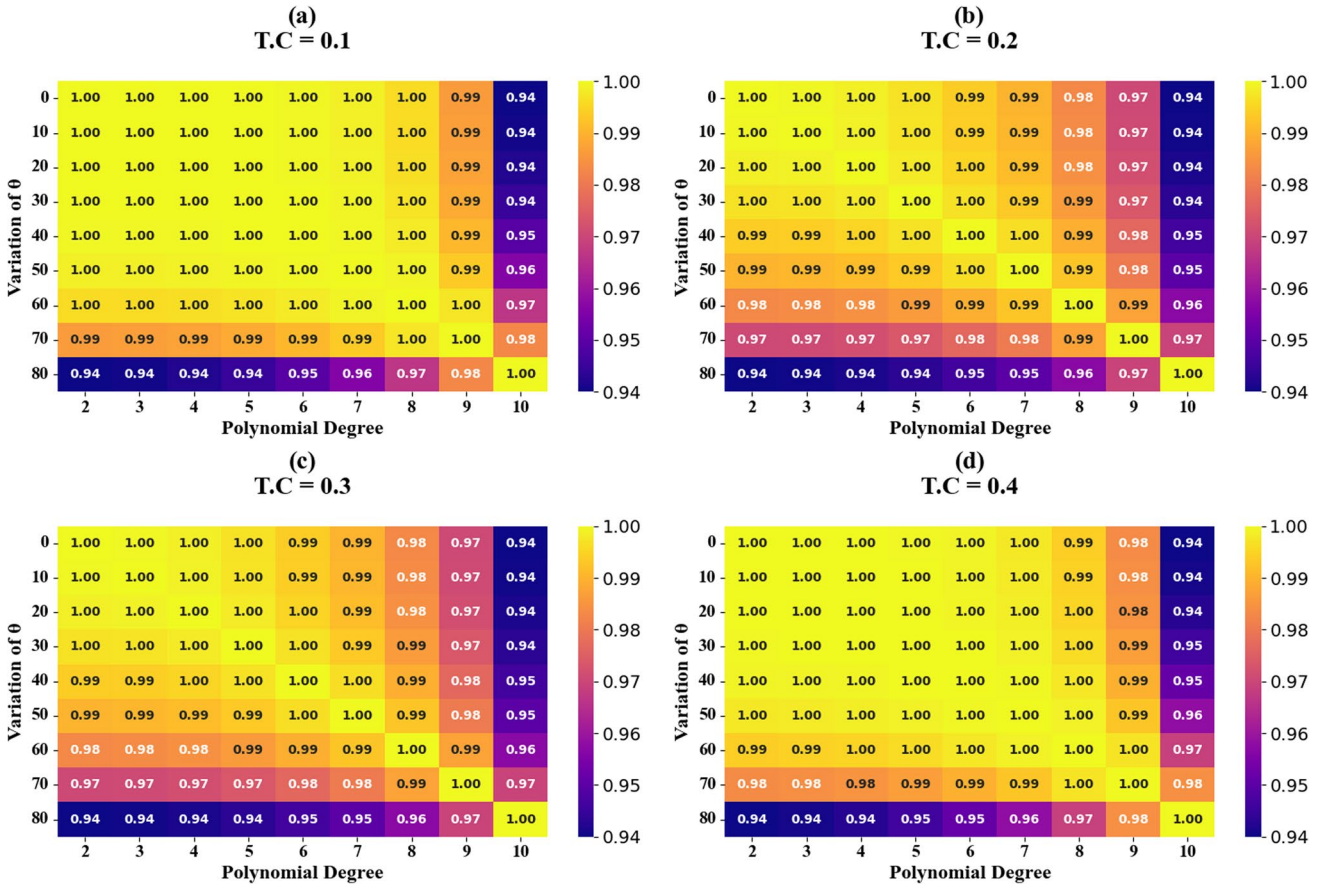

Fig. 22 displays HT showing the R^2 scores of XGR models across different combinations of θ

observed in Figs. 10 is indicative of a logic "1," while low transmittance, as seen in Figs. 8, corresponds to a logic "0." The ability to control the graphene conductive properties such as through electrical tuning of the graphene layer, allows the sensor to switch between high and low transmittance states. This capability facilitates a 2-bit encoding scheme.

Behaviour Prediction VIA XGBoost Regressor(XGR)

The development of a reliable sensor system for malaria detection presents a complex challenge due to the multifaceted nature of the optimization process and the extensive time required for structural refinement. This optimization process involves navigating a labyrinth of variables, each impacting the sensor's performance in unique ways. Identifying the precise effects of each structural parameter requires both patience and innovative thinking.Furthermore, the design process is further complicated by various external factors, such as environmental conditions and the characteristics of the virus, which can influence sensor performance. Despite the multidimensional nature of this challenge, machine learning (ML) models prove to be invaluable tools. These models not only assist in enhancing the sensor's structural design but also streamline the simulation phase. By leveraging artificial intelligence, researchers can accelerate the iterative redesign process and achieve faster solutions for concept implementation. ML models analyze vast datasets, uncovering relationships and patterns that traditional methods may overlook, thereby enabling engineers to make more informed decisions and enhance both the effectiveness and efficiency of malaria sensor designs.Among these models, XGBoost is renowned for its rapid computation, capacity to handle large datasets, and remarkable accuracy in regression tasks.[76]. XGBoost is an advanced ensemble machine learning technique that utilizes a highly optimized version of gradient boosting algorithms. Its primary methodology involves incrementally constructing an ensemble model by sequentially adding weak prediction models, generally decision trees. Each successive model is trained to address and reduce the residual errors of the preceding ensemble. This process integrates a loss function, which quantifies the prediction errors, with regularization techniques

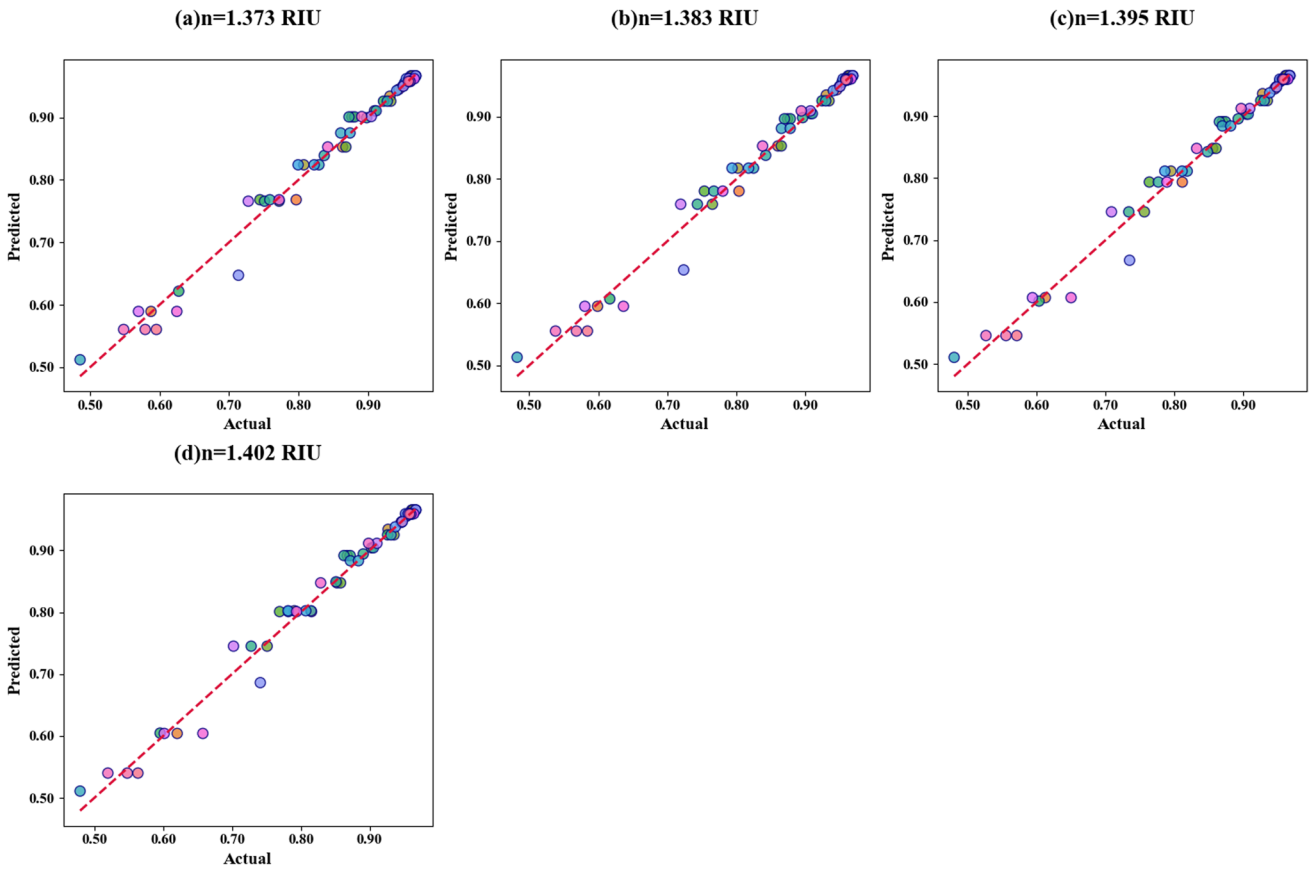

Fig. 23 illustrates scatter plots comparing the absorption values predicted by the XGR model with those obtained from simulations, focusing on the variation of RIs (n)

to mitigate overfitting. The additive approach combined with these optimizations enables XGBoost to enhance weak learners into a robust, highly predictive composite model[77].Optimizing the parameters of XGBoost is essential for attaining effective sensor design with excellent performance parameters. Key parameters include the learning rate, which determines the contribution of each individual decision tree to the overall ensemble model, and the regularization parameters, which control the model's complexity to mitigate the risk of overfitting. Techniques such as grid search and randomized search, which systematically evaluate numerous parameter combinations, are commonly employed to identify the optimal settings for a specific dataset and problem. Meticulous tuning of these parameters enables practitioners to refine XGBoost's performance and achieve the most accurate predictions from the model.Eq. (26) is employed to predict the expected outcome using the training dataset (M) for the XGBoost model. This dataset comprises pairs $\{A_i, B_i\}$, where A_i represents the independent variable and B_i represents the dependent variable in this context.

$$\hat{y}_i = \sum_{n=1}^{n} f_n(A_i) f_n \in F \tag{17}$$

Other equations for the regressor analysis include [78];

$$OBJ = \sum_{i=1}^{n} S(B_i, \widehat{B}_1) + \sum_{n=1}^{n} \Omega(f_n) \tag{18}$$

$$\Omega(c_1) = \gamma J + \frac{1}{2}\lambda \|w\|^2 \tag{19}$$

Equation (28) is employed to generate higher degree polynomial features for an independent variable.

$[1, A_i^1, A_i^2, \ldots A_i^V]$(20)

$$R^2 = \frac{\sum_{i=1}^{N} (PredictedTargetValue_i - ActualTargetValue_i)}{\sum_{i=1}^{N} \left(ActualTarget_i - AverageTargetValue\right)^2} \tag{21}$$

Detailed discussion is provided by [76, 79, 80]

In the first case,the investigation examines the efficacy of XGR models trained using diverse combinations of GCP and

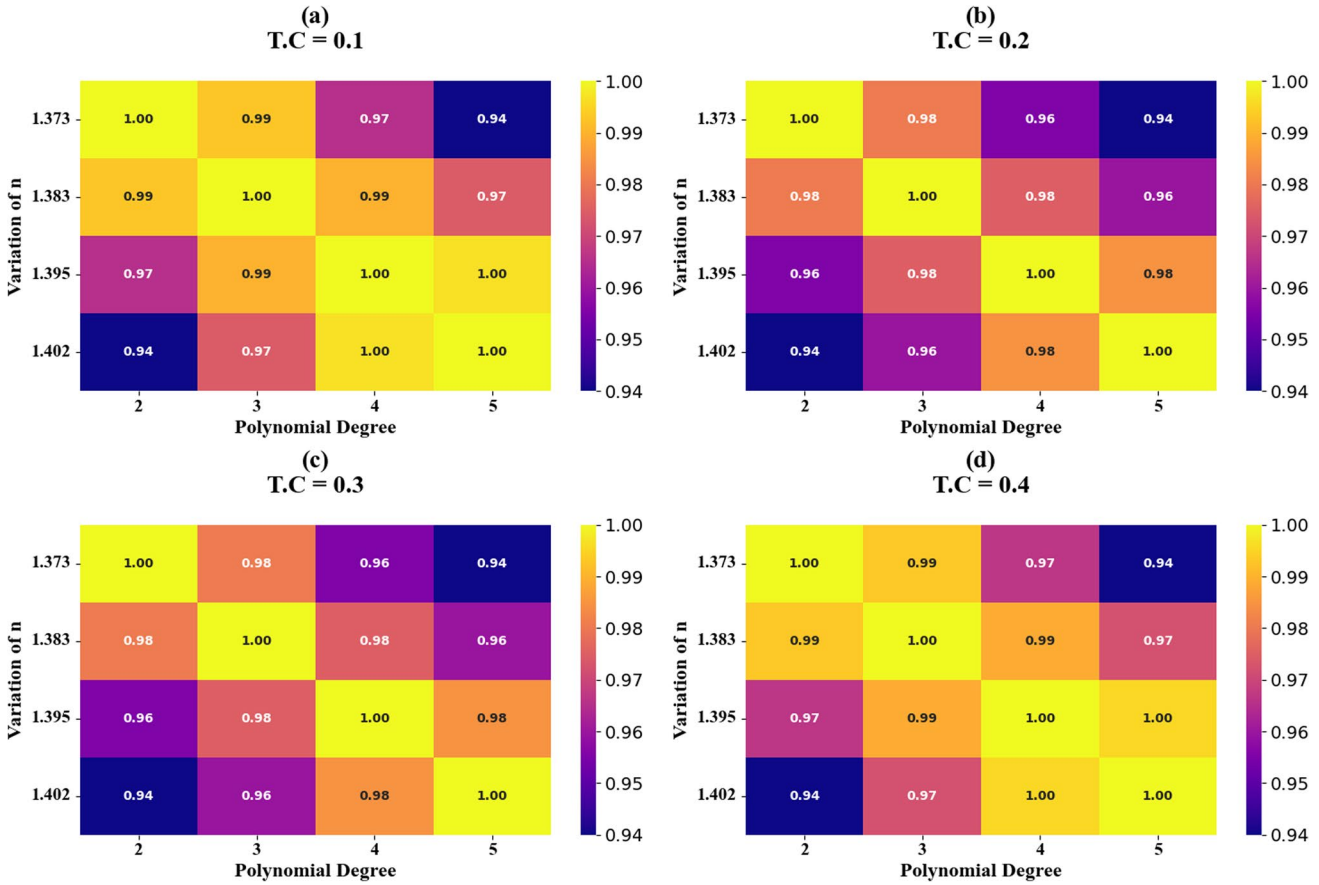

Fig. 24 displays HT showing the R^2 scores of XGR models across different combinations of n

polynomial degree parameters. The findings are visualized through a series of scatter plots (Figs. 11a-i) and heat maps (Figs. 12a-d). Analysis of the scatter plots reveals that for test cases (TC) ranging from 0.2 to 0.4, the models achieve R^2 scores between 99.6% and 100% (Figs. 11a-i). The heat map visualizations (Figs. 12a-d) demonstrate a clear trend in R^2 score improvement. For TC = 0.1 and TC = 0.4, R^2 scores increase from 96 to 100% (Figs. 12, respectively). Similarly, for TC = 0.2 and TC = 0.3, R^2 scores range from 94 to 100% (Figs. 12, respectively).

In the second case, the study systematically assesses the performance of XGR models trained with different combinations of the parameters C and polynomial degree. The findings are depicted through scatter plots (Figs. 13a-d) and heat maps (Figs. 14a-d). The scatter plots demonstrate that for test cases (TC) ranging from 0.1 to 0.2, the models achieve R^2 values between 99.0% and 99.2%. The heat maps reveal a consistent pattern of R^2 score improvement. Especially, for TC = 0.1, R^2 scores increase from 92 to 100%; for TC = 0.2 and TC = 0.3, the scores rise from 88 to 100%; and for TC = 0.4, R^2 scores vary between 91 and 100%.

For the third analysis, an evaluation of XGR model performance utilizing varied combinations of the parameters S and polynomial degree. Results are visualized through scatter plots (Figs. 15a-f) and heat maps (Figs. 16a-d). Scatter plot analysis indicates that for test cases (TC) in the range of 0.3 to 0.4, models achieve coefficient of determination (R^2) values between 99.7% and 99.8%. Heat map visualization demonstrates a consistent trend of R^2 score enhancement across different TC values. For TC = 0.1, R^2 scores increase from 93 to 100%. In the case of TC = 0.2, R^2 scores rise from 92 to 100%. When TC = 0.3, R^2 scores exhibit a range from 92 to 100%. Similarly, for TC = 0.4, R^2 scores vary between 93 and 100%.

In the fourth analysis, the performance of the XGR model was evaluated across various parameter combinations, precisely focusing on the parameters S and polynomial degree. The results are visualized using scatter plots (Figs. 17a-i) and heat maps (Figs. 18a-d). Scatter plot analysis indicates that for test cases (TC) within the range of 0.25 to 0.35, the models achieve R^2 values ranging from 99.3% to 99.7%. Heat map analysis demonstrates a consistent improvement in R^2 scores across different TC values. For TC = 0.1, R^2 scores increases from 94 to 100%. For TC = 0.2, R^2 scores improves from 92 to 100%. At TC = 0.3, R^2 scores ranges from 92 to 100%, and for TC = 0.4, R^2scores varies between 93 and 100%.

In the fifth analysis, the performance of the XGR model is assessed across a range of parameter configurations focusing on parameters H and polynomial degree. The evaluation results are presented through scatter plots (Figs. 19a-e) and heat maps (Figs. 20a-d). Scatter plot analysis demonstrates that for test cases (TC) within the interval of 0.15 to 0.45, the model attains R^2 values ranging from 99.4% to 99.9%. Heat map analysis further illustrates a consistent enhancement in R^2 scores across varying TC values. Notably, for TC = 0.1, R^2 scores improves from 96 to 100%. For TC = 0.2, R^2 scores increases from 94 to 100%. At TC = 0.3, R^2 scores ranges from 94 to 100%, and for TC = 0.4, R^2 scores fluctuates between 95 and 100%.

In the sixth analysis, the performance of the XGR model was systematically evaluated across a range of parameter configurations, specifically focusing on the parameters θ and polynomial degree. The evaluation results are presented through scatter plots (Figs. 21a-i) and heat maps (Figs. 22a-d). The scatter plot analysis reveals that for test cases (TC) within the interval of 0.25 to 0.35, the model consistently achieves R^2 values ranging from 99.8% to 100%. The heat map analysis further corroborates a uniform enhancement in R^2 scores across varying TC values. Notably, for TC = 0.1–0.4, the R^2 scores improve from 94 to 100%.

In the final case**,** the XGR model's performance was thoroughly assessed across various parameter settings, with a particular emphasis on RIs and polynomial degree. The findings are illustrated using scatter plots (Figs. 23a-d) and heat maps (Figs. 24a-d). The scatter plot analysis indicates that for test cases (TC) in the range of 0.35 to 0.45, the model consistently yields R^2 values between 99.9% and 100%. Additionally, the heat map analysis confirms a consistent increase in R^2 scores across different TC values. Particularly, for TC values between 0.1 and 0.4, R^2 scores improved from 94 to 100%.

Conclusion

In this study, we have presented the design and theoretical analysis of a tunable terahertz metasurface biosensor for malaria detection. The proposed sensor leverages the unique properties of graphene, gold, and silver to create a highly sensitive platform capable of detecting subtle changes in refractive index corresponding to different concentrations of malaria parasites in blood samples. Through rigorous electromagnetic simulations using COMSOL Multiphysics, we optimized various structural parameters including graphene chemical potential, resonator dimensions, and incident angle to achieve maximum sensitivity. The sensor demonstrated excellent performance metrics, including a maximum sensitivity of 429 GHzRIU^{-1}, a figure of merit up to 10.989 RIU^{-1}, and a detection limit as low as 0.115 RIU. These results indicate the sensor's potential for detecting malaria at different stages of infection. Furthermore, the XGBoost machine learning algorithm is integrated to predict sensor behaviour across various design parameters and demonstrates high R^2 scores exceeding 99%. The proposed sensor also showcases promise for 2-bit encoding applications. The combination of high sensitivity, tunability, and multi-functional capabilities makes this sensor design a promising candidate for practical malaria detection and other biomedical applications. Future work could focus on experimental validation of the proposed design, exploration of its performance with other biomarkers, and further optimization using advanced machine learning techniques.

Acknowledgements The authors extend their gratitude to the National Forensic Sciences University for permitting them to use the digital computer laboratory for this research and ICCR for the scholarship sponsorship.

Authors Contributions "Conceptualization, JW; Methodology, NM, AO, AB; Software; Validation, all authors; Writing—original draft preparation, All authors; Formal Analysis, NM, AO, AB; Writing—review and editing, All Authors; All authors have read and agreed to the published version of the manuscript."

Funding No funding.

Data Availability The data supporting the findings in this work are available from the corresponding author with a reasonable request.

Declarations

Ethical Approval (not applicable).

Competing Interests The authors declare no competing interests.

References

1. Naresh V, Lee N (2021) A review on biosensors and recent development of nanostructured materials-enabled biosensors. Sensors (Switzerland) 21(4):1–35. https://doi.org/10.3390/s21041109
2. Turner APF (2013) Biosensors: Sense and sensibility. Chem Soc Rev 42(8):3184–3196. https://doi.org/10.1039/c3cs35528d
3. M. B. Kulkarni, N. H. Ayachit, and T. M. Aminabhavi, "Recent Advancements in Nanobiosensors: Current Trends, Challenges, Applications, and Future Scope," *Biosensors*, vol. 12, no. 10. 2022. https://doi.org/10.3390/bios12100892.
4. J. Ahmed, "Electrospinning for the manufacture of biosensor components: A mini-review," *Med. DEVICES SENSORS*, vol. 4, no. 1, 2021, https://doi.org/10.1002/mds3.10136.
5. J. Wekalao, G. P. Srinivasan, S. K. Patel, and F. A. Al-zahrani, "Optimization of graphene-based biosensor design for haemoglobin detection using the gradient boosting algorithm for behaviour prediction".
6. V. Sanko and F. Kuralay, "Label-Free Electrochemical Biosensor Platforms for Cancer Diagnosis: Recent Achievements and Challenges," *Biosensors*, vol. 13, no. 3. 2023. https://doi.org/10.3390/bios13030333.

7. S. K. P. & A. A. Haitham Alsaif, Jacob Wekalao, Naim Ben Ali, Omar Kahouli, Jaganathan Logeshwaran, "Design and Optimization of a MXene-Based Terahertz Surface Plasmon Resonance Sensor for Malaria Detection," *Plasmonics*, 2024.
8. M. G. Daher, Y. Trabelsi, Y. K. Prajapati, A. Panda, N. M. Ahmed, and A. N. Z. Rashed, "Highly sensitive detection of infected red blood cells (IRBCs) with plasmodium falciparum using surface plasmon resonance (SPR) nanostructure," *Opt. Quantum Electron.*, vol. 55, no. 3, 2023, https://doi.org/10.1007/s11082-022-04466-1.
9. J. Wekalao, S. K. Patel, N. K. Anushkannan, O. Alsalman, J. Surve, and J. Parmar, "Design of ring and cross shaped graphene metasurface sensor for efficient detection of malaria and 2 bit encoding applications," *Diam. Relat. Mater.*, vol. 139, no. August, p. 110401, 2023, https://doi.org/10.1016/j.diamond.2023.110401.
10. Oyegoke OO et al (2022) Malaria diagnostic methods with the elimination goal in view. Parasitol Res 121(7):1867–1885. https://doi.org/10.1007/s00436-022-07512-9
11. R. R. D. Nana, N. L. Ngum, V. Makoge, N. Amvongo-Adja, J. Hawadak, and V. Singh, "Rapid diagnostic tests for malaria diagnosis in Cameroon: impact of histidine rich protein 2/3 deletions and lactate dehydrogenase gene polymorphism," *Diagn. Microbiol. Infect. Dis.*, vol. 108, no. 1, 2024, https://doi.org/10.1016/j.diagmicrobio.2023.116103.
12. Zeleke MT et al (2023) Diagnostic performance of PfHRP2/pLDH malaria rapid diagnostic tests in elimination setting, northwest Ethiopia. PLOS Glob Public Heal 3(7):e0001879. https://doi.org/10.1371/journal.pgph.0001879
13. Green MR, Sambrook J (2018) The basic polymerase chain reaction (PCR). Cold Spring Harb Protoc 2018(5):338–345. https://doi.org/10.1101/pdb.prot095117
14. C. Chicharro *et al.*, " Molecular Diagnosis of Leishmaniasis in Spain: Development and Validation of Ready-To-Use Gel-Form Nested and Real-Time PCRs To Detect Leishmania spp. ," *Microbiol. Spectr.*, vol. 11, no. 3, 2023, https://doi.org/10.1128/spectrum.03354-22.
15. Choosang K et al (2024) A dot-blot ELISA preliminary evaluation using PvMSP1-42 recombinant protein as antigen for serological diagnosis of Plasmodium vivax infection in Thailand. Eur J Microbiol Immunol. https://doi.org/10.1556/1886.2024.00008
16. F. Maghsood, A. Ghorbani, H. Yadegari, F. Golsaz-Shirazi, M. M. Amiri, and F. Shokri, "SARS-CoV-2 nucleocapsid: Biological functions and implication for disease diagnosis and vaccine design," *Reviews in Medical Virology*, vol. 33, no. 3. 2023. https://doi.org/10.1002/rmv.2431.
17. K. Ou *et al.*, "Advances in Meta-Optics and Metasurfaces: Fundamentals and Applications," *Nanomaterials*, vol. 13, no. 7. 2023. https://doi.org/10.3390/nano13071235.
18. Kuznetsov AI et al (2024) Roadmap for Optical Metasurfaces. ACS Photonics. https://doi.org/10.1021/acsphotonics.3c00457
19. Moitra P et al (2023) Electrically Tunable Reflective Metasurfaces with Continuous and Full-Phase Modulation for High-Efficiency Wavefront Control at Visible Frequencies. ACS Nano 17(17):16952–16959. https://doi.org/10.1021/acsnano.3c04071
20. Y. Yang *et al.*, "Integrated metasurfaces for re-envisioning a near-future disruptive optical platform," *Light: Science and Applications*, vol. 12, no. 1. 2023. https://doi.org/10.1038/s41377-023-01169-4.
21. S. Yadav, B. Kumar, and S. Kaushik, "Emergent 2D materials beyond graphene: Plausible role in biomedical applications," *Appl. Surf. Sci. Adv.*, vol. 18, 2023, https://doi.org/10.1016/j.apsadv.2023.100512.
22. M. Seredych, M. Alhabeb, B. Anasori, and Y. Gogotsi, "(Invited) High-Temperature Behaviors of MXenes," *ECS Meet. Abstr.*, vol. MA2018–01, no. 15, pp. 1136–1136, 2018, https://doi.org/10.1149/ma2018-01/15/1136.
23. El Ghazaly A et al (2021) Ultrafast, One-Step, Salt-Solution-Based Acoustic Synthesis of Ti3C2MXene. ACS Nano 15(3):4287–4293. https://doi.org/10.1021/acsnano.0c07242
24. J. A. Kumar *et al.*, "Methods of synthesis, characteristics, and environmental applications of MXene: A comprehensive review," *Chemosphere*, vol. 286, 2022, https://doi.org/10.1016/j.chemosphere.2021.131607.
25. H. Goel *et al.*, "Mxene-based nanocomposites for biosensing: Recent developments and future prospects," *FlatChem*, vol. 42. 2023. https://doi.org/10.1016/j.flatc.2023.100576.
26. N. H. Solangi, N. M. Mubarak, R. R. Karri, S. A. Mazari, and A. S. Jatoi, "Advanced growth of 2D MXene for electrochemical sensors," *Environ. Res.*, vol. 222, 2023, https://doi.org/10.1016/j.envres.2023.115279.
27. Seekaew Y, Kamlue S, Wongchoosuk C (2023) Room-Temperature Ammonia Gas Sensor Based on Ti3C2Tx MXene/Graphene Oxide/CuO/ZnO Nanocomposite. ACS Appl Nano Mater 6(10):9008–9020. https://doi.org/10.1021/acsanm.3c01637
28. M. Bilal, A. K. Singh, H. M. N. Iqbal, and G. Boczkaj, "Enzyme-conjugated MXene nanocomposites for biosensing and biocatalysis acuities," *Chemical Engineering Journal*, vol. 474. 2023. https://doi.org/10.1016/j.cej.2023.145020.
29. Khan K et al (2023) Recent Progress in Emerging Novel MXenes Based Materials and their Fascinating Sensing Applications. Small. https://doi.org/10.1002/smll.202206147
30. Tang Z et al (2020) Phosphorus Science-Oriented Design and Synthesis of Multifunctional Nanomaterials for Biomedical Applications. Matter 2(2):297–322. https://doi.org/10.1016/j.matt.2019.12.007
31. Y. Cai *et al.*, "An electrochemical biosensor based on graphene intercalated functionalized black phosphorus/gold nanoparticles nanocomposites for the detection of bacterial enzyme," *Microchem. J.*, vol. 193, 2023, https://doi.org/10.1016/j.microc.2023.109255.
32. Nangare S, Patil P (2023) Black Phosphorus Nanostructure Based Highly Sensitive and Selective Surface Plasmon Resonance Sensor for Biological and Chemical Sensing: A Review. Crit Rev Anal Chem 53(1):1–26. https://doi.org/10.1080/10408347.2021.1927669
33. B. Li *et al.*, "Black Phosphorus, a Rising Star 2D Nanomaterial in the Post-Graphene Era: Synthesis, Properties, Modifications, and Photocatalysis Applications," *Small*, vol. 15, no. 8. 2019. https://doi.org/10.1002/smll.201804565.
34. Suk SH, Seo SB, Cho YS, Wang J, Sim S (2024) Ultrafast optical properties and applications of anisotropic 2D materials. Nanophotonics 13(2):107–154. https://doi.org/10.1515/nanoph-2023-0639
35. Anju S, Ashtami J, Mohanan PV (2019) Black phosphorus, a prospective graphene substitute for biomedical applications. Mater Sci Eng, C 97:978–993. https://doi.org/10.1016/j.msec.2018.12.146
36. Wekalao J, Alsalman O, Shobhit RM (2024) Graphene biosensor design based on glass substrate for forensic detection of illicit drugs. Opt Quantum Electron. https://doi.org/10.1007/s11082-024-06690-3
37. J. Muheki, J. Wekalao, H. B. Albargi, M. Jalalah, and A. H. M. Almawgani, "A Graphene Gold Metasurface Inspired Surface Plasmon Resonance Sensor Designed for Terahertz Applications in Sensing and Detection of Heavy Metals in Water," 2024.
38. J. Wekalao, H. B. Albargi, S. K. Patel, M. Jalalah, and A. H. M. Almawgani, "Terahertz Optical Ultrasensitive Glucose Detection Using Graphene and Silver Surface Plasmon Resonance Metasurfaces for Biomedical Applications," *Plasmonics*, no. 123456789, 2024, https://doi.org/10.1007/s11468-024-02278-5.
39. J. Wekalao, A. K. U, H. B. Albargi, M. Jalalah, A. H. M. Almawgani, and A. Armghan, "Graphene and Gold Metasurface-Based Terahertz Surface Plasmon Resonance Sensor for

Explosive Detection," *Plasmonics*, 2024, https://doi.org/10.1007/s11468-024-02229-0.
40. A. H. M. Almawgani, J. Wekalao, S. K. Patel, A. Alzahrani, and H. S. Gumaih, "Design and Development of a Split Ring Resonator and Circular Disc Metasurface Based Graphene / Gold Surface Plasmon Resonance Sensor for Illicit Drugs Detection," *Plasmonics*, no. 123456789, 2024, https://doi.org/10.1007/s11468-024-02306-4.
41. S. K. P. & F. A. A.-Z. N. K. Anushkannan, Jacob Wekalao, "Design of Encoded and Tunable Graphene-Gold Metasurface-Based Surface Plasmon Resonance Sensors for Glucose Detection in the Terahertz Regime," *Plasmonics*, 2024.
42. J. Wekalao, N. Mandela, J. Muheki, and A. Zaid, "Design and Analysis of a Terahertz Metasurface - Based Refractive Index Sensor for Hemoglobin Detection With Behaviour Prediction Using Polynomial Regression," *Plasmonics*, no. 123456789, 2024, https://doi.org/10.1007/s11468-024-02445-8.
43. I. Ben Soltane, F. Dierick, B. Stout, and N. Bonod, "Generalized Drude–Lorentz Model Complying with the Singularity Expansion Method," *Adv. Opt. Mater.*, 2024, https://doi.org/10.1002/adom.202400093.
44. Potts JR, Dreyer DR, Bielawski CW, Ruoff RS (2011) Graphene-based polymer nanocomposites. Polymer 52(1):5–25. https://doi.org/10.1016/j.polymer.2010.11.042
45. Johnson DW, Dobson BP, Coleman KS (2015) A manufacturing perspective on graphene dispersions. Curr Opin Colloid Interface Sci 20(5–6):367–382. https://doi.org/10.1016/j.cocis.2015.11.004
46. J. Wekalao, O. Alsalman, H. Patel, R. Manvani, and S. K. Patel, *Swift detection of heavy metals in water by encoded graphene–gold-metasurface sensor*, vol. 56, no. 7. Springer US, 2024. https://doi.org/10.1007/s11082-024-07140-w.
47. Catania F et al (2021) A review on recent advancements of graphene and graphene-related materials in biological applications. Applied Sciences (Switzerland) 11(2):1–21. https://doi.org/10.3390/app11020614
48. S. K. Patel, J. Wekalao, N. Mandela, and F. A. Al-Zahrani, "Design of encoded graphene-gold metasurface-based circular ring and square sensors for brain tumor detection and optimization using XGBoost algorithm," *Diam. Relat. Mater.*, vol. 148, no. June, p. 111439, 2024, https://doi.org/10.1016/j.diamond.2024.111439.
49. Ullah S et al (2021) Graphene transfer methods: A review. Nano Res 14(11):3756–3772. https://doi.org/10.1007/s12274-021-3345-8
50. H. Nguyen Bich and H. Nguyen Van, "Promising applications of graphene and graphene-based nanostructures," *Advances in Natural Sciences: Nanoscience and Nanotechnology*, vol. 7, no. 2. 2016. https://doi.org/10.1088/2043-6262/7/2/023002.
51. J. Liu, S. Bao, and X. Wang, "Applications of Graphene-Based Materials in Sensors: A Review," *Micromachines*, vol. 13, no. 2. 2022. https://doi.org/10.3390/mi13020184.
52. T. Das, B. K. Sharma, A. K. Katiyar, and J. H. Ahn, "Graphene-based flexible and wearable electronics," *J. Semicond.*, vol. 39, no. 1, 2018, https://doi.org/10.1088/1674-4926/39/1/011007.
53. D. J. Joe, E. Park, D. H. Kim, I. Doh, H. C. Song, and J. Y. Kwak, "Graphene and Two-Dimensional Materials-Based Flexible Electronics for Wearable Biomedical Sensors," *Electronics (Switzerland)*, vol. 12, no. 1. 2023. https://doi.org/10.3390/electronics12010045.
54. N. P. Jacob, W. Ashokkumar, and N. S. K. Patel, "Design and Analysis of a Plasmonic Metasurface - Based Graphene Sensor for Highly Sensitive and Label - Free Detection of COVID - 19 Biomarkers," *Plasmonics*, no. 123456789, 2024, https://doi.org/10.1007/s11468-024-02442-x.
55. K. A. & A. A. Meshari Alsharari, Jacob Wekalao, Shobhit K. Patel, Arun Kumar U., "Enhanced Sensing Efficiency of Ultra-Narrow Band Graphene-Based Surface Plasmon Resonance Refractive Index Sensor for Biochemical Applications and Environmental Monitoring," *Plasmonics*, 2024.
56. J. Wekalao, O. Alsalman, N. A. Natraj, J. Surve, J. Parmar, and S. K. Patel, "Design of Graphene Metasurface Sensor for Efficient Detection of COVID-19," *Plasmonics*, no. 123456789, 2023, https://doi.org/10.1007/s11468-023-01946-2.
57. Aliqab K, Wekalao J, Alsharari M, Armghan A, Agravat D, Patel SK (2023) Designing a Graphene Metasurface Organic Material Sensor for Detection of Organic Compounds in Wastewater. Biosensors 13(8):1–16. https://doi.org/10.3390/bios13080759
58. J. Wekalao, S. K. Patel, O. Alsalman, J. Surve, N. K. Anushkannan, and J. Parmar, "Waterborne Bacteria Detecting Highly Sensitive Graphene Metasurface Based Cost-Efficient and Efficient Refractive Index Sensors," *Plasmonics*, no. 123456789, 2023, https://doi.org/10.1007/s11468-023-01983-x.
59. S. K. Patel, J. Wekalao, O. Alsalman, J. Surve, J. Parmar, and S. A. Taya, "Development of surface plasmon resonance sensor with enhanced sensitivity for low refractive index detection," *Opt. Quantum Electron.*, vol. 55, no. 11, 2023, https://doi.org/10.1007/s11082-023-05265-y.
60. O. Alsalman, J. Wekalao, U. Arun Kumar, D. Agravat, J. Parmar, and S. K. Patel, "Design of Split Ring Resonator Graphene Metasurface Sensor for Efficient Detection of Brain Tumor," *Plasmonics*, no. 123456789, 2023, https://doi.org/10.1007/s11468-023-02002-9.
61. Wekalao J et al (2023) Graphene-Based THz Surface Plasmon Resonance Biosensor for Hemoglobin Detection Applicable in Forensic Science. Plasmonics. https://doi.org/10.1007/s11468-023-02146-8
62. S. K. Patel, J. Wekalao, H. B. Albargi, M. Jalalah, and A. H. M. Almawgani, "Design and Simulation of Metasurface - Enhanced Graphene Biosensors for Cancer Biomarker Detection," *Plasmonics*, no. 123456789, 2024, https://doi.org/10.1007/s11468-024-02224-5.
63. Shewchuk JR (2002) Delaunay refinement algorithms for triangular mesh generation. Comput Geom Theory Appl 22(1–3):21–74. https://doi.org/10.1016/S0925-7721(01)00047-5
64. Shewchuk JR (2014) Reprint of: Delaunay refinement algorithms for triangular mesh generation. Comput Geom Theory Appl 47(7):741–778. https://doi.org/10.1016/j.comgeo.2014.02.005
65. C. Kittel, "Introduction to Solid State Physics, 8th edition," *Wiley Sons, New York, NY*, 2004.
66. Jain PK, Lee KS, El-Sayed IH, El-Sayed MA (2006) Calculated absorption and scattering properties of gold nanoparticles of different size, shape, and composition: Applications in biological imaging and biomedicine. J Phys Chem B 110(14):7238–7248. https://doi.org/10.1021/jp057170o
67. A. Kumar, P. Verma, and P. Jindal, "Machine learning approach to surface plasmon resonance sensor based on MXene coated PCF for malaria disease detection in RBCs," *Optik (Stuttg).*, vol. 274, 2023, https://doi.org/10.1016/j.ijleo.2023.170549.
68. A. Abbaszadeh and S. Rash-Ahmadi, "A surface plasmon resonance sensor based on photonic crystal fiber composed of magnesium fluoride and graphene layers to detect aqueous solutions," *Opt. Quantum Electron.*, vol. 56, no. 6, 2024, https://doi.org/10.1007/s11082-024-06853-2.
69. K. Aliqab, J. Wekalao, M. Alsharari, A. Armghan, D. Agravat, and S. K. Patel, "Designing a Graphene Metasurface Organic Material Sensor for Detection of Organic Compounds in Wastewater," *Biosensors*, vol. 13, no. 8, 2023, https://doi.org/10.3390/bios13080759.
70. A. H. M. Almawgani, J. Wekalao, S. K. Patel, A. Alzahrani, H. S. Gumaih, and A. Armghan, "Optimization of Graphene-Based Square Slotted Surface Plasmon Resonance Refractive Index

Biosensor for Accurate Detection of Pregnancy," *Plasmonics*, no. 123456789, 2024, https://doi.org/10.1007/s11468-024-02290-9.
71. and M. W. H. Tazin Fatema, Sumaya Arafin, Sohanur Rahman, "Numerical analysis and early detection of Plasmodium falciparum using a high performance plasmonic biosensor with an external sensing approach," *Appl. Opt.*, vol. 63, no. 10, 2024.
72. Nijhum JM, Ahmed T (2023) Highly sensitive quasi-D-shaped photonic crystal fiber biosensor designed for the detection of RBC parasitized by Plasmodium falciparum for the early diagnosis of malaria. Opt Contin 2(6):1315. https://doi.org/10.1364/optcon.489682
73. R. Singh, W. Cao, I. Al-Naib, L. Cong, W. Withayachumnankul, and W. Zhang, "Ultrasensitive terahertz sensing with high- Q Fano resonances in metasurfaces," *Appl. Phys. Lett.*, vol. 105, no. 17, 2014, https://doi.org/10.1063/1.4895595.
74. S. K. Saini and S. K. Awasthi, "Sensing and Detection Capabilities of One-Dimensional Defective Photonic Crystal Suitable for Malaria Infection Diagnosis from Preliminary to Advanced Stage: Theoretical Study," *Crystals*, vol. 13, no. 1, 2023, https://doi.org/10.3390/cryst13010128.
75. R. Cheng, L. Xu, X. Yu, L. Zou, Y. Shen, and X. Deng, "High-sensitivity biosensor for identification of protein based on terahertz Fano resonance metasurfaces," *Opt. Commun.*, vol. 473, 2020, https://doi.org/10.1016/j.optcom.2020.125850.
76. P. Zhang, Y. Jia, and Y. Shang, "Research and application of XGBoost in imbalanced data," *Int. J. Distrib. Sens. Networks*, vol. 18, no. 6, 2022, https://doi.org/10.1177/15501329221106935.
77. T. Chen and C. Guestrin, "XGBoost: A scalable tree boosting system," in *Proceedings of the ACM SIGKDD International Conference on Knowledge Discovery and Data Mining*, 2016, pp. 785–794. https://doi.org/10.1145/2939672.2939785.
78. Patel SK et al (2022) Encoding and Tuning of THz Metasurface-Based Refractive Index Sensor with Behavior Prediction Using XGBoost Regressor. IEEE Access 10:24797–24814. https://doi.org/10.1109/ACCESS.2022.3154386
79. Wang C, Deng C, Wang S (2020) Imbalance-XGBoost: leveraging weighted and focal losses for binary label-imbalanced classification with XGBoost. Pattern Recognit Lett 136:190–197. https://doi.org/10.1016/j.patrec.2020.05.035
80. W. Su *et al.*, "An XGBoost-Based Knowledge Tracing Model," *Int. J. Comput. Intell. Syst.*, vol. 16, no. 1, 2023, https://doi.org/10.1007/s44196-023-00192-y.

Publisher's Note Springer Nature remains neutral with regard to jurisdictional claims in published maps and institutional affiliations.

Springer Nature or its licensor (e.g. a society or other partner) holds exclusive rights to this article under a publishing agreement with the author(s) or other rightsholder(s); author self-archiving of the accepted manuscript version of this article is solely governed by the terms of such publishing agreement and applicable law.

View publication stats